



www.sciencemag.org/content/342/6162/1237435/suppl/DC1

Supplementary Materials for

The Innate Growth Bistability and Fitness Landscapes of Antibiotic-Resistant Bacteria

J. Barrett Deris, Minsu Kim, Zhongge Zhang, Hiroyuki Okano, Rutger Hermsen,
Alexander Groisman, Terence Hwa

Corresponding author. E-mail: hwa@ucsd.edu

Published 29 November 2013, *Science* **342**, 1237435 (2013)

DOI: 10.1126/science.1237435

This PDF file includes:

Materials and Methods
Figs. S1 to S19
Tables S1 to S5
References (71–121)

Other Supplementary Material for this manuscript includes the following:

(available at www.sciencemag.org/content/342/6162/1237435/suppl/DC1)

Movies S1 and S2

Supplementary Materials

for

The innate growth bistability and fitness landscapes of antibiotic resistant bacteria

Deris *et al.* (2013)

Materials and Methods.....	2
Supplementary Discussion (Theoretical Analysis).....	6
Figures S1-S19.....	24
Online Movie Legends (S1, S2).....	52
Supplementary Tables (S1-S5).....	53
Supplementary References (71-121).....	61

Supplementary Materials

SUPPLEMENTARY METHODS

Strain construction

All of the strains used in this study are derived from *Escherichia coli* K12 strain MG1655 and described in table S1. The region containing *lacI*, *lacZ* and *lacY* genes was deleted using the method of Datsenko and Wanner (71). Construction of strain Lac2 (also known as EQ37, in which *lacI* and *lacY* were deleted and *lacZ* is driven by $P_{Ltet-O1}$) is described in Scott *et al* (16). DNA oligos used for construct and strain preparation are described in table S4. For all experiments, strains stocks were stored at -80 °C. Plates were streaked with stock strains within two weeks of use and stored at 4 °C.

Construction of a new chromosomal *lacZ* reporter strain. The synthetic and Crp-independent $P_{Llac-O1}$ promoter (-60 to +47, relative to the transcriptional start site) was amplified from pZE12 (72) and substituted for $P_{Ltet-O1}$ in pKD13- $P_{Ltet-O1}$ (16), yielding pKD13- $P_{Llac-O1}$. Using the method of Datsenko and Wanner (71), the promoter plus the upstream Km^r gene ($Km^r:P_{Llac-O1}$) in pKD13- $P_{Llac-O1}$ was integrated into the chromosome to replace the *lacI* gene and the native *lac* promoter (including the 5' UTR of *lacZ*) of MG1655 deleted for *lacY* (57). The resultant strain, in which *lacZ* is driven by $P_{Llac-O1}$ and both *lacI* and *lacY* are deleted, is named as EQ5.

Chromosomal incorporation of resistance markers. The $P_{Llac-O1}$ promoter described above was substituted for $P_{Ltet-O1}$ in pKDT- $P_{Ltet-O1}$ (57), yielding pKDT- $P_{Llac-O1}$. The *cat* structural gene, encoding the protein responsible for chloramphenicol resistance, was amplified from pZA31 (72) using forward primer Cat-Kpn-F and reverse Cat-Bam-R. The PCR products were gel purified, digested with *KpnI* and *BamHI*, then ligated into the same sites of pKDT- $P_{Llac-O1}$, yielding pKDT- $P_{Llac-O1}$ -*cat*. Present in this plasmid, the construct $Km^r:rrnBT:P_{Llac-O1}$ -*cat* was amplified using primers Placat-P1 and Placat-P2. The Placat-P1 contains a 51 bp region that is homologous to the intergenic region (272nd to 222nd nucleotides relative to the start codon of *ycaD*) between *ycaC* and *ycaD* while Placat-P2 contains a 50 bp region that is reverse complemented to the *ycaC/ycaD* intergenic region located between 116th and 67th nucleotides relative to the start codon of *ycaD*. The PCR products were gel purified and then electroporated into MG1655 cells that carried pKD46 (71) expressing the λ -Red recombinase. The cells were incubated with shaking at 37 °C for 1 hour and then applied onto LB + Km agar plates. The plates were incubated at 30 °C overnight. The Km^r colonies were verified for the substitution for the *ycaC/ycaD* intergenic region between 222nd and 116st nucleotides relative to the start codon of *ycaD* by colony PCR and subsequently by sequencing. The $Km^r:rrnBT:P_{Llac-O1}$ -*cat* construct was moved to background strain EQ4 with P1 phage transduction (73), and colonies were selected for resistance to Km and Cm on agar plates.

The Km^r gene was flipped out using the standard method (71). The resultant strain is named EQ75, also known as Cat1 in the main text.

To make chromosomal *cat* driven by $P_{Ltet-O1}$ (72), the same *cat* gene as above was cloned into *KpnI/BamHI* sites downstream of $P_{Ltet-O1}$ in pKDT_ $P_{Ltet-O1}$ (57), yielding pKDT_ $P_{Ltet-O1}$ -*cat*. The cassette “ Km^r :*rrnBT*: $P_{Llac-O1}$ -*cat*” from this plasmid was incorporated into the same *ycaC/ycaD* site as described above. This strain is named EQ92, also referred to as Cat2 in the main text.

As expected, the cell with the chromosomal $P_{Llac-O1}$ -*cat* was highly resistant to Cm. To vary Cm resistance levels using site-directed mutagenesis, we modified the region containing the ribosome binding site (RBS) in $P_{Llac-O1}$ by inserting 4 nucleotides (TCCT) immediately downstream of RBS or/and changing one or two nucleotides in RBS (see table S3). The modified $P_{Llac-O1}$ promoters (containing various altered RBS) together with *cat* were moved to the chromosome at the same location as described above. The resulting strains are referred to as Cat3 through Cat6.

To make the chromosomal *tetA* driven by $P_{Llac-O1}$, the *tetA* gene was cloned from the transposon Tn10 (also known as *tetA(B)* (74)) and subsequently substituted for *cat* in pKDT_ $P_{Llac-O1}$ -*cat* (see above), yielding pKDT_ $P_{Llac-O1}$ -*tetA*. Similarly as described above, The cassette “ Km^r :*rrnBT*: $P_{Llac-O1}$ -*tetA*” was integrated into the *ycaC/ycaD* locus.

Chromosomal deletion of *motA* and chromosomal integration of $P_{Ltet-O1}$ -*gfp*. The *motA* gene deletion in strain JW1879-2 (*E. coli* Genetic Stock Center, Yale Univ.), in which a Km^r gene is substituted for the *motA* gene, was transferred to EQ4 and Cat1 by P1 transduction (73), and Km^r was then removed as described above to yield EQ4m and Cat1m (table S1).

To make the chromosomal GFP driven by $P_{Ltet-O1}$, a *gfpmut3b* structural gene (75) was cloned downstream of $P_{Ltet-O1}$ in pKD13_ $P_{Ltet-O1}$ (57), yielding pKD13T_ $P_{Ltet-O1}$ -*gfp*. The construct “ Km^r :*rrnBT*: $P_{Ltet-O1}$ -*gfp*” present in this plasmid was integrated into the *intS/yfdG* intergenic region of the MG1655 chromosome as previously described (76). The “ Km^r : *rrnBT*: $P_{Llac-O1}$ -*gfp*” construct was then P1-transduced into the Cat1m background to create strain GCat1m.

Microfluidic device fabrication

Microfluidic devices were fabricated by molding silicone elastomer (PDMS Silygard 184, Dow Corning) to the master molds (28), consisted of two layers of cross-linked epoxy (Su-8s, MicroChem) patterned by negative phototransparency masks (FineLine Imaging, CO) on silicon wafers (fig. S4A). The layer for growth chambers (~1.5 μm) was deposited first using SU-8 2002 and processed according to the manufacturer’s manual. On top of the first layer, the second layer for channels (~25 μm) was made using SU-8 2025 (side view).

PDMS was mixed 1:15 ratio of catalyst and resin, poured to the master mold, degassed for 30 min and cured in an 80 °C oven for 90 min. After the elastomer was peeled off the mold, inlet and outlet holes were punched. Then, the device was boiled in 1% HCl solution for 1 hour, attached to No.1 microscope cover glass (pre-cleaned with ethanol) and baked in the 80 °C oven overnight for maximum binding.

CAT assays

We used two separate CAT assays in this study, the radiometric assay and the spectrophotometric CAT assay as described below. The spectrophotometric assay was used to obtain an estimate of the absolute CAT activity per OD₆₀₀ in strain Cat1 (table S2) and Cat2, and to quantify the CAT activities of strain Cat1 when growth was inhibited by tetracycline (Fig. 3C). We used the radiometric assay (performed on Cat1 and Cat3-Cat6) to determine the CAT activities of strains Cat3-Cat6 relative to Cat1. Relative CAT activities of all strains Cat1-Cat6 are given in the bottom of Fig. 4B.

Sample collection and cell permeabilization for CAT assays. We collected samples (at OD₆₀₀ ~ 0.15 – 0.4) from cultures growing in minimal medium after at least 3 generations of exponential growth and stored them at -80 °C for assays the following day. After thawing samples we added an equal amount of extraction buffer (0.2 M Tris, pH 8.0, 10 mM EDTA, and for the radiometric assay, an additional 40 mM β-mercaptoethanol). We then added toluene to 1% by volume, vortexed vigorously for 15 seconds (or 10 seconds for radiometric assay) and allowed cultures to incubate at room temperature for 15 minutes before performing the assays as described below (either spectrophotometric or radiometric). To identify the range in our assay over which CAT activity was proportional to CAT protein levels, we diluted samples with various volumes of permeabilized wild type cells (EQ4) and assayed activity. CAT activities reported in this study are within the linear dose-response window as identified above.

Spectrophotometric CAT assays. We used essentially the method of Shaw (77). The assay was performed by aspirating 15 μL permeabilized sample into 135 μL reaction buffer inside the cuvette of a Thermo Scientific Genesys 20 spectrophotometer preheated to 37 °C. The standard reaction buffer contained 150 μL of 4 mg/ml 5,5'-dithiobis-(2-nitro- benzoic acid) suspended in Tris/HCl, pH 8.0, 60 μL each of 20 mM Acetyl-CoA and 5 mM Cm, and 1.08 mL deionized H₂O. We recorded absorbance A₄₁₂ every 6 seconds using VISIONlite software (Thermo Scientific) between minutes 4-8 of the reaction (absorbance increased linearly during the reaction for at least 10 minutes). Reported activity was taken as the slope of the absorbance over time (minus the slope of a blank sample lacking CAT), divided by the final OD₆₀₀ of cells in the reaction volume (U/OD₆₀₀). To obtain the *in vitro* activity estimate for strain Cat1 (table S2), we performed a total of 7 assays from samples collected from two replicate cultures on different days with fresh media and reagents to obtain a value repeatable to within ~10%.

Radiometric CAT assays. Radiometric CAT assay was performed essentially as described by Seed and Sheen (78). Briefly, after samples thawed they were diluted to

OD₆₀₀ = 0.32 (Bio-Rad SmartSpec Plus) by the medium used for the culture. The assay was performed by adding 50 μ L permeabilized sample to 75 μ L reaction mixture preincubated at 37 °C for 5 min to give final concentrations of 100 mM Tris/HCl, pH8.0, 100 μ M [³H] chloramphenicol (25 μ Ci/ μ mol), 240 μ M butyryl CoA, 1% (vol/vol) ethanol. After incubation at 37°C for 30 min, the reaction was terminated by addition of 250 μ L xylene, and mixed vigorously by vortexing. After centrifugation, 80% of the xylene phase was extracted twice with an equal volume of 10 mM Tris/HCl, pH7.5, 1 mM EDTA. The remaining organic phase was counted in a scintillation counter.

β -Galactosidase assay

Chloramphenicol-sensitive strains Lac1 (EQ5) and Lac2 (EQ37) express LacZ constitutively from the chromosome (table S1). We grew these strains in M63 minimal media + 0.4% glucose in presence and absence of Cm inside 20 mm diameter glass tubes, as described above in the section “batch culture growth.” Experimental culture tubes contained up to 10 μ M chloramphenicol to retard growth. During exponential growth (with and without Cm), four to six samples (~200 μ L) were collected from each growing culture (OD₆₀₀ = 0.1 to ~0.8), fast frozen on dry ice and stored at -80°C prior to the assay. β -Galactosidase activity was measured at 37°C by the traditional Miller method (79). The LacZ activity per volume of cell culture (OD) was obtained as the slope of the plot of LacZ activity levels (Δ OD₄₂₀/min/ml) versus OD₆₀₀ to give Miller Units used in Fig. 3C.

Supplementary Discussion

THEORETICAL ANALYSIS

We present here in detail our mathematical model for antibiotic-resistant growth, including the origins of Eqs. [1]-[4] which define the model in the main text, and describe how growth bistability and plateau-shaped fitness landscapes emerge from these equations. In doing so we outline the details upon which these phenomena depend, in both a qualitative and quantitative sense (e.g., the dependence of MIC and MCC predicted by physical parameters in the model). A key concept in the model is the "growth-mediated feedback" that arises due to global effects of cellular growth state on gene expression. In particular, the feedback describes the way that growth rate affects expression of proteins offering antibiotic resistance.

We will not restrict our discussion to the behavior of a specific antibiotic or resistance enzyme, but we will apply the general model to the specific antibiotics and respective resistance mechanisms used in our experiments (chloramphenicol, tetracycline, and minocycline). We will examine translation inhibiting antibiotics and resistance conferred by enzymes that modify the antibiotic (inactivation), or pump the drug out of the cell and away from its target (efflux). We will begin with the simplest equations that realize our basic assumptions and then add complexity to these models when necessary to better describe physiological conditions in experiments; in many cases, we will see that the simplest descriptions capture the experimental findings without further elaboration. Whenever possible, we will also provide independent estimates of the parameters used in the model.

1. Modeling cell growth in the presence of antibiotics, for both antibiotic- sensitive and resistant cells

1.1 Effects of antibiotics on translation rate

Whether bacteriostatic or bactericidal, sub-inhibitory concentrations of translation-inhibiting antibiotics often allow exponential growth in bacteria, albeit at reduced rates (80–82). We concern ourselves here with this simple exponential growth, and model the effect of the antibiotic as reducing the average translation rate γ , due to the direct binding between the ribosome (Rb) and antibiotic (a) (22). We assume that the concentration of antibiotic-bound ribosomes $[Rb \cdot a]$ reaches equilibrium rapidly, characterized by a dissociation constant, K_D . Then the fraction of unaffected ribosomes is

$$\frac{[Rb]}{[Rb]_{\text{total}}} = \frac{1}{1 + [a]_{\text{int}} / K_D}, \quad [\text{S1}]$$

where $[Rb]$ and $[Rb]_{\text{total}} \equiv [Rb] + [a \cdot Rb]$ are respectively the unaffected and total

ribosome concentration, and $[a]_{\text{int}}$ is the internal antibiotic concentration. Here we have described equilibrium antibiotic-ribosome binding without cooperativity for simplicity, but this form is in fact the correct one for the antibiotics used in this work Cm, Tc, and Mn (22, 83). Assuming that the drug-bound ribosomes do not translate at all, the total translation rate in a cell is given by $\gamma_0 \cdot [Rb] = \gamma \cdot [Rb]_{\text{total}}$, where

$$\gamma \equiv \frac{\gamma_0}{1 + [a]_{\text{int}} / K_D} \quad [\text{S2}]$$

is referred to as the average translation rate, and γ_0 is the translation rate in the absence of drug. (NB, here and throughout this work, a subscript of "0" indicates a value in the absence of drug).

1.2 The relation between translation rate and growth rate, and the emergence of the half-inhibition concentration

Under steady exponential growth, recent work by Scott *et al.* (16) has established a Monod-like expression for the growth rate,

$$\lambda = \lambda^{\text{max}} \frac{\nu}{\gamma + \nu} \quad [\text{S3}]$$

where γ is the drug-dependent average translation rate as defined in Eq. [S2], ν is related to the rate of nutrient utilization and is fixed for a given saturating nutrient medium, and λ^{max} is the maximum growth rate achievable with a theoretically best possible nutrient (see fig. S9). In drug-free medium, the above becomes

$$\lambda_0 = \lambda_0^{\text{max}} \frac{\nu}{\gamma_0 + \nu} \quad [\text{S4}]$$

where $\lambda_0^{\text{max}} \approx 2.85$ 1/hr (16). Taking the ratio of Eqs. [S3] and [S4], and using Eq. [S2] for γ/γ_0 yields

$$\lambda = \frac{\lambda_0}{1 + [a]_{\text{int}} / I_{50}} \quad [\text{S5}]$$

where

$$I_{50} = K_D \cdot \lambda_0^{\text{max}} / \lambda_0, \quad [\text{S6}]$$

is the predicted half-inhibition concentration, the internal antibiotic concentration that reduces growth rate by 50%.

Reports of *in vitro* measurements of K_D for Cm-ribosome binding in *E. coli* range from 0.6 to 2.7 μM (22, 84). For wild-type *E. coli* (EQ4) cells growing in glucose minimal media, $\lambda_0 \approx 0.67$ hr⁻¹. Eq. [S6] thus predicts I_{50} to be of several micromolar ($2.8 \leq [I_{50}] \leq 12$ μM) during Cm-inhibited growth, as long as the dominant mode of

action for the antibiotic is to inhibit translation via ribosomal binding.

1.3 The relation between intra- and extra- cellular antibiotic concentrations in the absence antibiotic resistance expression

Inverting Eq. [S5] leads to the result that the relative doubling time ($\tau / \tau_0 \equiv \lambda_0 / \lambda$) increases linearly with the drug concentration (see Eq. [4] in Fig. 3 of the main text). The observed linear relationship in Fig. 3D is consistent with this prediction if the antibiotic concentration in the medium, denoted by $[a]_{\text{ext}}$, is proportional to $[a]_{\text{int}}$ over some range. The latter is expected generally if antibiotic enters the cell via passive diffusion, with an influx rate

$$J_{\text{influx}} = \kappa \cdot ([a]_{\text{ext}} - [a]_{\text{int}}) \quad [\text{S7}]$$

where κ is the membrane permeability, and exits the cell via native low-affinity efflux

$$J_{\text{efflux}} \approx V_{\text{native}}^{\text{max}} \cdot [a]_{\text{int}} / K_{\text{native}}, \quad [\text{S8}]$$

assuming Michaelis kinetics for efflux. Note that low-affinity efflux is common in antibiotic-susceptible cells and this endogenous efflux is not associated with clinically relevant antibiotic resistance (41). The passive uptake of antibiotics into cells is well-established for Cm (41), Tc (85), and many others (86). Balancing the influx and efflux in the steady state (and neglecting dilution due to cell growth¹), we obtain the linear relation

$$[a]_{\text{ext}} = [a]_{\text{int}} \cdot \left(1 + \frac{V_{\text{native}}^{\text{max}}}{\kappa \cdot K_{\text{native}}} \right), \quad [\text{S9}]$$

which leads to an effective half-inhibition concentration $\tilde{I}_{50} \equiv I_{50} \cdot \left(1 + V_{\text{native}}^{\text{max}} / \kappa \cdot K_{\text{native}} \right)$, describing external antibiotic concentration when growth rate is reduced by half. Since endogenous efflux of antibiotics is weak for cells grown in minimal media (87), we expect $V_{\text{native}}^{\text{max}} / (\kappa \cdot K_{\text{native}}) < 1$ for Cm (41) and tetracyclines (87, 88) in our experiments.

The data of Fig. 3D give a value of 5.5 μM Cm for the half-inhibition concentration. This is in the range estimated above for I_{50} , suggesting that efflux may indeed be negligible for Cm at low concentrations in minimal medium.

1.4 The relation between intra- and extra- cellular antibiotic concentrations in the presence of antibiotic resistance expression

A key qualitative result in this section is captured by Eq. [S12], from which we will see that the relation between intra- and extracellular antibiotic concentration is marked by two distinct regimes in the presence of an enzyme offering antibiotic resistance. We

¹ Typical influx rates are much larger than growth rate, at least ~200-fold higher for drugs used in this study (See (88) and table S2)). However, when dilution due to growth is non-negligible, and in the absence of efflux, the dilution may have important consequences for bacterial growth (54).

assume an enzyme E is expressed at a concentration $[E]$ in the steady state, with the effect of reducing the intracellular pool of the active antibiotic. Whether the protein functions as an efflux pump (as in Tc-TetA system) or as enzyme inactivating the drug (as in the Cm-CAT system studied in the main text), we assume the enzymatic process can be simply described by Michaelis-Menten kinetics, with the rate of antibiotic removal given by

$$J_{\text{removal}} = \frac{V_{\text{max}}}{1 + K_m/[a]_{\text{int}}} \quad [\text{S10}]$$

with affinity K_m , and $V_{\text{max}} \equiv k_{\text{cat}} \cdot [E]$. Assuming that the antibiotic enters the cell via passive diffusion (Eq. [S7]), the balance of influx and removal leads to the following relation between the external and internal drug concentrations:

$$[a]_{\text{ext}} = [a]_{\text{int}} + \frac{V_{\text{max}}/\kappa}{1 + K_m/[a]_{\text{int}}} . \quad [\text{S11}]$$

This relation is sketched in Fig. 3B, and the origin of the approximate threshold-linear form is motivated in its caption. Mathematically, the two regimes are simply

$$[a]_{\text{int}} \approx \begin{cases} [a]_{\text{ext}} / (1 + V_{\text{max}}/\kappa K_m) & \text{for } [a]_{\text{ext}} \ll V_{\text{max}}/\kappa \\ [a]_{\text{ext}} - V_{\text{max}}/\kappa & \text{for } [a]_{\text{ext}} \gg V_{\text{max}}/\kappa \end{cases} \quad [\text{S12}]$$

This threshold-linear behavior, when combined with the growth-mediated feedback as described below, provides the mechanism for bistability in antibiotic resistance. An important dimensionless parameter that arises whenever passive influx is balanced by Michaelis-Menten efflux kinetics is $V_{\text{max}}/(\kappa K_m)$, a term that was previously found useful in describing antibiotic resistance (89), albeit in a different context. Strong effect of drug relief is realized for $V_{\text{max}}/K_m \gg \kappa$, where $[a]_{\text{int}} \ll [a]_{\text{ext}}$ for a broad regime of drug concentrations $[a]_{\text{ext}} \ll V_{\text{max}}/\kappa$.

We mention as an aside that if growth-mediated feedback did not play a role, then Eqs. [S11] and [S5] would determine growth rate. With V_{max} as a constant, the growth rate is expected to decrease smoothly with increasing external antibiotic concentrations, similar to the response of wild-type cells. We present the results of this no-feedback model fig. S17 (dashed lines) to compare to growth rate data from our CAT-expressing strains. The behavior of the no-feedback model cannot account for the observed abrupt drops in growth rate even at a qualitative level.

1.5 The effect of growth-mediated feedback in cells expressing antibiotic resistance

The above relation between the internal and external drug concentration assumes a constant expression level of the enzyme providing drug resistance, i.e., constant V_{max} , as the external drug concentration is varied. However, sub-inhibitory concentrations of

antibiotics generically lead to altered expression of proteins (12, 13, 16, 17, 43, 90) unless very specific regulatory mechanisms such as negative feedback control are involved (57). In this study, we investigate the unregulated (or “constitutive”) expression of resistance mechanisms, because (i) in many instances the expression of drug resistance is known not to involve specific regulatory mechanisms (25), and (ii) *de novo* evolution of novel drug resistance mechanisms is likely to proceed without drug-specific regulation.

The expression levels of unregulated proteins have been shown to depend linearly on the growth rate under sub-inhibitory doses of translation-inhibiting antibiotics (16). This is seen in Fig. 3C for constitutively expressed LacZ and CAT under Cm- and Tc- inhibited growth, respectively. The V_{\max} of the enzyme under sub-inhibitory growth can hence be written in terms of the growth rate λ , and the V_{\max} and growth rate in the absence of drug, V_0 and λ_0 respectively, as

$$V_{\max} = V_0 \cdot \frac{\lambda}{\lambda_0} \quad [\text{S13}]$$

Combining Eq. [S13] with [S11] then gives the full expression relating $[a]_{\text{ext}}$ and $[a]_{\text{int}}$ at different growth rates λ :

$$[a]_{\text{ext}} = [a]_{\text{int}} + \frac{\lambda}{\lambda_0} \cdot \frac{V_0 / \kappa}{1 + K_m / [a]_{\text{int}}} . \quad [\text{S14}]$$

Eliminating λ / λ_0 using Eq. [S5] gives

$$[a]_{\text{ext}} = [a]_{\text{int}} + \frac{V_0}{\kappa} \cdot \frac{1}{1 + [a]_{\text{int}} / I_{50}} \cdot \frac{1}{1 + K_m / [a]_{\text{int}}} . \quad [\text{S15}]$$

Eq. [S15] can be inverted to predict the internal drug concentration for every external drug concentration, given the chemical properties of the drug (K_m , κ , and I_{50}), and the drug resistance expression system that defines V_0 . The value of $[a]_{\text{int}}$ can subsequently be used (via Eq. [S5]) to predict the relative growth rate (λ / λ_0) for the given external drug concentration.

2. Model predictions and their sensitivity to biophysical parameters

Since the relative growth rate (λ / λ_0) only depends on $[a]_{\text{int}} / I_{50}$, and I_{50} itself does not depend on the concentrations of the drug or drug resistance enzyme (see Eq. [S6]), we shall rewrite Eq. [S15] in terms of $a_i \equiv [a]_{\text{int}} / I_{50}$ and $a_e \equiv [a]_{\text{ext}} / I_{50}$, with

$$a_e = a_i \cdot \left(1 + \frac{1}{1 + a_i} \cdot \frac{\rho}{1 + \sigma \cdot a_i} \right) \quad [\text{S16}]$$

Here, we have introduced two dimensionless parameters: the 'resistance efficacy'

$$\rho \equiv V_0 / (\kappa \cdot K_m) \quad [\text{S17}]$$

which indicates the efficiency of the drug-resistance enzyme in unit of drug influx, and the 'saturability'

$$\sigma \equiv I_{50} / K_m \quad [\text{S18}]$$

which characterizes the extent to which the activity of the drug-resistance enzyme is saturated at growth-inhibiting concentrations of the antibiotic. The relative growth rate,

$$\frac{\lambda}{\lambda_0} = \frac{1}{1 + a_i} \quad [\text{S19}]$$

is now completely specified by a_e , ρ , and σ .

For a given strain growing in a medium with a particular antibiotic and expressing some degree of resistance to that antibiotic, *in vitro* parameters uniquely determine the values of σ and ρ ; see tables S2, S5 for biochemical parameters of the specific systems studied in this work (Cm-CAT, Tc-TetA, Mn-TetA). In the main text we describe how experimentally tuning the parameter ρ affects cell growth. Here we characterize the generic behavior of the system, i.e., the dependence of cell growth at different external concentrations as defined by Eq. [S16], with σ and ρ as arbitrary parameters.

2.1 Criteria for the coexistence of multiple growth phases

2.1.1 Origin of coexistence

Plotting the relation between a_e and a_i as defined by Eq. [S16] for a range of ρ values, we see that for sufficiently large ρ , there exists a range of external antibiotic concentration a_e for which multiple a_i values correspond to a single a_e for a given ρ (fig. S18A). Since each internal concentration a_i corresponds to a unique growth rate according to Eq. [S19], multiple solutions here correspond to the coexistence of multiple growth phases. As indicated in fig. S18B for a fixed set of σ and ρ , the appearance of the local extrema a_e^{\min} and a_e^{\max} define the boundaries of external drug concentrations within which multiple growth phases coexist (for a particular strain/condition that correspond to the chosen values of σ and ρ).

The two local extrema divide the solution of Eq. [S16] into three branches of *internal* antibiotic concentration: low, high, and intermediate, for $a_i < a_i^*$, $a_i > a_i^\dagger$, and $a_i^* < a_i < a_i^\dagger$ respectively, as indicated in fig. S18B, with the red curve segment indicating the intermediate region. Figs. S18C–D show the dependence of the growth rate λ on a_e , by converting a_i to λ using Eq. [S19]. Comparing fig. S18B and 17D shows that the low- a_i region corresponds to sub-inhibitory growth, and the high- a_i region corresponds to growth inhibition, though the growth rate in this region is small but finite according to the

model. In the section below, we show that a_e^{\max} and a_e^{\min} correspond to the theoretical MIC and MCC respectively (Eqs. [S28] and [S39]) for parameter values relevant to this study. The intermediate- a_i region is dynamically unstable (and hence irrelevant) according to deterministic kinetic analysis (see discussion surrounding Eq. [S44]).

2.1.2 Phase diagram and the onset of coexistence at the critical resistance efficacy

Fig. S18A shows that the local extrema disappear for sufficiently small ρ , i.e. for $\rho < \rho_c$; the disappearance of the phase of coexistence in the phase diagram of Fig. 4B reflects this transition for small V_0 (which controls the magnitude of ρ in our experiments). The bifurcation point where the extrema just appears, commonly referred to as the “critical point”, can be obtained from the following defining conditions,

$$\frac{\partial a_e(a_{i,c}, \rho_c, \sigma)}{\partial a_i} = \frac{\partial^2 a_e(a_{i,c}, \rho_c, \sigma)}{\partial a_i^2} = 0 \quad [\text{S20}]$$

and solving for the critical values ρ_c and $a_{i,c}$ as a function of σ . We find the minimal resistance efficacy that produces phase coexistence to be

$$\rho_c(\sigma) = \left[\sigma^{1/3} + 1 + \sigma^{-1/3} \right]^3. \quad [\text{S21}]$$

The form of $\rho_c(\sigma)$ is plotted in fig. S19A, and the minimum at $\rho_c^{\min} = 27$ when $\sigma = 1$ indicates that phase coexistence occurs most readily when $K_m \approx I_{50}$; i.e., relatively low values of resistance efficacy ρ already give rise to coexistence. For the systems investigated in our experiments, σ is of order one and coexistence is predicted to occur for $\rho \gtrsim 29$ (see I_{50} and K_m values in tables S2, S5). For the Cm-CAT system, this corresponds to a critical value of $(V_0 / \kappa)_{\text{crit}} \cong 350 \mu\text{M}$ based on the parameters in table S2.

2.1.3 Critical external antibiotic concentration

Similarly, solving Eq. [S21] for $a_{i,c}$ gives

$$a_{i,c} = \sigma^{-1/3} + \sigma^{-2/3} \quad [\text{S22}]$$

yielding the critical external concentration at the bifurcation point

$$a_{e,c} = \left(1 + \sigma^{-1/3} \right)^3 \quad [\text{S23}]$$

or

$$[a]_{\text{ext}}^{\text{crit}} = \left(\sqrt[3]{I_{50}} + \sqrt[3]{K_m} \right)^3 \quad [\text{S24}]$$

which takes the value $[\text{Cm}]_{\text{ext}}^{\text{crit}} \approx 67 \mu\text{M}$ for the Cm-CAT system (see table S2).

For $\rho < \rho_c(\sigma)$, there is a unique solution a_i for each external concentration a_e , and a

homogeneous growth phase is expected. For $\rho > \rho_c(\sigma)$, a_e^{\max} and a_e^{\min} define the MIC and MCC respectively, as described above. We next describe their dependences on ρ , which is readily probed in experiments by changing the basal expression level of antibiotic resistance (V_0 in the model).

2.2 Interpretation and prediction of the Minimum Inhibitory Concentration (MIC)

To solve for the MIC, we look for the maximum of a_e as defined by Eq. [S16]. The value of a_i giving the maximum, a_i^* (as illustrated in fig. S18B), is found to obey the following equation,

$$\sigma \cdot (a_i^*)^2 = 1 + (1 + a_i^*)^2 \cdot (1 + \sigma a_i^*)^2 / \rho. \quad [\text{S25}]$$

Solving for a_i^* in powers of $1/\rho$ (and identifying a_i^* as the smaller of the two solutions), we obtain

$$a_i^* \approx \frac{1 + b/\rho}{\sqrt{\sigma}} \quad [\text{S26}]$$

where $b = (1 + \sigma^{-1/2})^2 \cdot (1 + \sigma^{1/2})^2 / 2$, giving

$$a_e^{\max} \approx \frac{\rho}{(1 + \sigma^{1/2})^2} + \sigma^{-1/2} + \frac{1}{\rho} \frac{(1 + \sigma^{1/2})^4}{2\sigma^{3/2}} + \dots \quad [\text{S27}]$$

from Eq. [S16]. Since $\rho_c \geq 27$, then for $\rho > \rho_c(\sigma)$ where the maximum exists, the sub-leading terms in $1/\rho$ are negligible; see fig. S19B–C that illustrate this for the Cm-CAT system ($\sigma \approx 0.46$, table S2). Thus, the MIC is predicted to be

$$\text{MIC} = a_e^{\max} \cdot I_{50} \approx \frac{V_0 / \kappa}{\left(1 + \sqrt{K_m / I_{50}}\right)^2} + \sqrt{K_m \cdot I_{50}} \quad [\text{S28}]$$

which becomes for the Cm-CAT system

$$\text{MIC} \approx 0.16 \cdot V_0 / \kappa + 8 \mu\text{M} \quad [\text{S29}]$$

The approximate linear dependence of the MIC on the basal expression level of drug resistance is verified by the data (circled numbers) shown in Fig. 4B.

2.3 Abrupt drop in growth rate and the plateau-shaped fitness landscape

In fig. S19B, we show the accuracy of the approximation for a_i^* . Equation [S26] is seen to approximate the full solution very well until very close the critical point (compare the solid black and dashed red lines). In the limit $\rho \gg b$, which corresponds to $\rho \gtrsim 4 \cdot \rho_c(\sigma)$ for the Cm-CAT system, the leading expression in Eq. [S26] (dashed black line)

$$a_i^* \approx \frac{1}{\sqrt{\sigma}} = \sqrt{K_m / I_{50}} \quad [\text{S30}]$$

already suffices. In this limit, Eq. [S16] is reduced to

$$a_e \approx a_i \cdot \rho \cdot \frac{1}{1 + a_i} \cdot \frac{1}{1 + \sigma \cdot a_i} . \quad [\text{S31}]$$

The growth rate at a_e^{\max} becomes independent of ρ , with

$$\lambda^* = \frac{\lambda_0}{1 + a_i^*} \approx \frac{\lambda_0}{1 + \sqrt{K_m / I_{50}}} , \quad [\text{S32}]$$

giving

$$\lambda^* \approx 0.4 \cdot \lambda_0 \quad [\text{S33}]$$

for the Cm-CAT system (fig. S19D). As there is no growth for concentrations above MIC, λ^* represents the size of the abrupt drop in the growth rate as the drug concentration is increased beyond the MIC. Growth rate data are consistent with the approximate independence of λ^* on the level of drug resistance activity V_0 as long as resistance efficacy $V_0 / (\kappa \cdot K_m)$ is not too close to the critical point ρ_c ; see e.g., Figs. 4C and 5A.

2.4 Criteria for dormancy and the Minimum Coexistence Concentration (MCC)

To solve for the MCC, we look for the minimum of Eq. [S16], a_e^{\min} , which occurs at the internal concentration $a_i = a_i^\dagger$ (see fig. S18B for illustration). It is also necessary to establish the conditions on parameters ρ and σ for which growth is effectively completely inhibited when $a_i \geq a_i^\dagger$ (such that the system has a dormant state in addition to the growing state). We obtain a_i^\dagger as the larger solution to Eq. [S25]. In the limit $[a]_{\text{int}} \gg K_m$, or equivalently $a_i \gg \sigma^{-1}$, we find

$$a_i^\dagger \approx \sqrt{\frac{\rho}{\sigma}} \cdot \left(1 - \frac{\sigma^{1/2} + \sigma^{-1/2}}{\rho^{1/2}} \right) \quad [\text{S34}]$$

to the first sub-leading order in $\rho^{-1/2}$, with the value of the minimum given by

$$a_e^{\min} \approx \sqrt{\frac{\rho}{\sigma}} \left(2 - \frac{\sigma^{1/2} + \sigma^{-1/2}}{\rho^{1/2}} \right) \quad [\text{S35}]$$

This approximation is in good agreement with the full solution of a_e^{\min} as shown in fig.

S19E-F for $\sigma = 0.46$ (for the Cm-CAT system). To determine whether or not a dormant state exists for $a_e > a_e^{\min}$, we find the predicted growth rate at this boundary ($a_i = a_i^\dagger$)

$$\lambda_\dagger = \frac{\lambda_0}{1 + a_i^\dagger} \approx \frac{\lambda_0}{\sqrt{\rho/\sigma} - \sigma^{-1}} \quad [\text{S36}]$$

The growth rate takes on low values, $\lambda_\dagger / \lambda_0 < 0.1$ (practically undetectable), for antibiotic resistant strains in this work until very close to the critical point; see fig. S19G. When $\sigma > 2$ (and $\rho > \rho_c(\sigma)$ to ensure coexistence) this predicted growth rate can be appreciably greater than zero and is approximately

$$\frac{\lambda_\dagger}{\lambda_0} \approx \sqrt{\frac{\sigma}{\rho}} = \sqrt{\frac{I_{50} \cdot \kappa}{V_0}} \quad [\text{S37}]$$

Equation [S37] suggests that growth rate along this “slow growth” branch can be increased arbitrarily by decreasing the ratio ρ/σ ; however, bistability disappears for $\rho < \rho_c(\sigma) = (\sigma^{-1/3} + 1 + \sigma^{1/3})$ as in Eq. [S20]. The growth rate at $a_i = a_i^\dagger$ with $\rho = \rho_c(\sigma)$ gives the maximum value λ_\dagger may take at a_e^{\min} :

$$\lambda_\dagger^{\max}(\sigma) = \frac{\lambda_0}{1 + \sigma^{-1/3} + \sigma^{-2/3}} \quad [\text{S38}]$$

(with $\rho = \rho_c(\sigma)$). This value is small (e.g. $\lambda_\dagger^{\max} \leq \lambda_0/3$) when $\sigma \leq 1$, or equivalently when $I_{50} \leq K_m$. The I_{50} and K_m parameters for the CAT and TetA systems used in this study (corresponding to $\sigma = 0.46$ and 0.4 respectively), give $\lambda_\dagger^{\max} / \lambda_0 \approx 0.25$ at the critical point such that cell growth in the “high” $[a]_{\text{int}} > I_{50} \cdot a_e^{\min}$ branch of drug concentration is virtually completely inhibited. Thus, the minimal *coexistence* concentration a_e^{\min} corresponds practically to the Minimal *Coexistence* Concentration (MCC), and a_e^{\max} corresponds to MIC as claimed above (Eq. [S28]). Using the approximate form Eq. [S35] and with $\rho/\sigma \gg 1$, the MCC is predicted to increase with the square root of drug resistance activity (V_0), as

$$\text{MCC} = a_e^{\min} \cdot I_{50} \approx 2 \cdot \sqrt{I_{50} \cdot V_0 / \kappa} - (I_{50} + K_m) \quad [\text{S39}]$$

Additionally, we can write the MCC in terms of MIC for strains with high levels of resistance. In the limit $\text{MIC} \gg \sqrt{I_{50} \cdot K_m}$, MIC becomes approximately proportional to V_0 / κ (to zero order in $\sqrt{I_{50} \cdot K_m} / \text{MIC}$, Eq. [S28]). Then with Eq. [S39] one finds a simple expression for MCC in terms of MIC

$$\text{MCC} \approx 2 \cdot \left(\sqrt{K_m} + \sqrt{I_{50}} \right) \cdot \sqrt{\text{MIC}} \quad [\text{S40}]$$

Thus, it is possible to predict the range of concentrations over which growing and non-growing cells coexist without explicitly knowing or fitting the value of parameter V_0 / κ .

2.5 Stochasticity cannot generate the plateau-shaped fitness landscape

We examine here whether the stochastic expression of CAT from its constitutive promoter, when combined with the nonlinear relation between external and internal C_m (Fig. 3B), might be sufficient to explain the plateau-shaped fitness landscape without invoking growth-mediated feedback. In this scenario, a small (stochastic) decrease in CAT expression could lead to a large increase in intracellular antibiotic concentration, thereby arresting growth. A similar model was previously used to describe the transition between growing and dormant states in natural persistence (91), in which the stochastic expression of a “toxin” gene (*hipA*) induced cells to enter a dormant state, with the lifetime of the dormant state determined by HipA concentration in a threshold-linear manner. We find that while such a model can in principle give rise to heterogeneity in growth rates among a population, it cannot reproduce the abrupt drop in growth rate observed at the MIC: the average growth rate is still expected to decrease smoothly as a function of drug concentration.

This can be understood by a simple mathematical analysis: an abrupt drop in growth rate at the MIC manifests itself as a divergence in the average doubling time of the population $\frac{\partial \tau}{\partial [A]_{\text{ext}}} \rightarrow \infty$, which can be rewritten as $\frac{\partial \tau}{\partial [A]_{\text{ext}}} = \frac{\partial \tau}{\partial [A]_{\text{int}}} \cdot \frac{\partial [A]_{\text{int}}}{\partial [A]_{\text{ext}}}$. Because the relation between doubling time and *intracellular* antibiotic concentration is continuous (Eq. [4], leading to the result in Fig. 3D), the observation of an abrupt jump would require

$$\frac{\partial [A]_{\text{int}}}{\partial [A]_{\text{ext}}} \rightarrow \infty \quad [\text{S41}]$$

i.e., the divergence must come from a discontinuity in the relation between $[A]_{\text{int}}$ and $[A]_{\text{ext}}$. However, the latter relation is fixed by the well-characterized kinetics of the CAT enzyme, which is given by the solution to Eq. [S11] (red line in Fig. 3B), and clearly lacks any discontinuity in the absence of growth-mediated feedback. Even in the extreme case where the relation between $[A]_{\text{int}}$ and $[A]_{\text{ext}}$ is exactly of the threshold-linear form, it is still continuous (dashed grey line of Fig. 3B); the derivative has a jump but still is not divergent. Therefore, including stochastic variation in this model cannot give rise to the abrupt drop in growth rate at the MIC, i.e., the plateau-shaped fitness landscape.

2.6 Constitutive expression of drug resistance and other forms of growth-mediated feedback

In our analysis we assumed constitutive expression of drug resistance. Aside from being the simplest system to characterize, CAT is indeed most often expressed constitutively in

Gram⁻ bacteria inside Tn9 and elsewhere (24). This scenario also occurs naturally in *integrons*, in which many unregulated resistance genes are placed under the control of a single high-activity constitutive promoter (25). Resistance genes in resistant clinical isolates have also been found to be under the control of constitutive promoters (27). But for a protein whose expression is specifically regulated, e.g. at the transcriptional or translational level, the growth-rate dependence need not be linear as in Fig. 3C (17, 57). In the simplest approximation one can modify Eq. [S13] to the form

$$V_{\max} = V_0 \cdot (\lambda / \lambda_0)^n, \quad n \geq 0. \quad [\text{S42}]$$

Deriving the consequences of this relation is beyond the scope of the current work, but we mention here some key results: First, growth bistability and plateau-shaped fitness still occur for a broad range of the (ρ, σ) -parameter space, but the criterion Eq. [S21] for the occurrence of the critical point depends on the value n . With the modification in Eq. [S42], one can show that a_e^{\max} still increases linearly with resistance efficacy ρ for strong resistance, and hence approximately $\text{MIC} \sim V_0 / \kappa$ as before, although the slope and intercept in Eq. [S28] will depend nontrivially on n also. Interestingly, linear dependence of the empirical MIC on V_0 has also been reported for bacterial resistance to other antibiotics (89, 92). This is likely a result of the generic relationship between $[a]_{\text{int}}$ and $[a]_{\text{ext}}$, in which Michaelis-Menten kinetics of resistance activity (Eq. [S10]) are balanced by diffusive influx (Eq. [S7]). Then, assuming cell growth is inhibited at some characteristic internal drug concentration (corresponding empirically to $[a]_{\text{ext}} = \text{MIC}$), simple flux balance dictates a linear relationship between this $[a]_{\text{int}}$ and MIC (Eq. [S10], $[a]_{\text{ext}} \gg V_0 / \kappa$).

The MCC is more sensitive than MIC to the form of the feedback, with the result

$$\text{MCC} \sim \left(V_0 / \kappa \right)^{\frac{1}{n+1}} \quad [\text{S43}]$$

For $n > 1$, the feedback is more cooperative and the MCC is reduced. Thus, the onset of growth bistability occurs at lower antibiotic concentrations as the cooperativity in feedback (n) is increased. Conversely, for weak feedback (in the limit $n \rightarrow 0$) the region of bistability shrinks as $\text{MCC} \sim V_0 / \kappa$ approaches the MIC.

2.7 Stability analysis

Here we perform a stability analysis of the deterministic model whose steady states are captured by Eqs. [S16] and [S19]. Specifically, we address the qualitative question regarding the stability in the coexistence regime where multiple solutions are obtained. By themselves, Eqs. [S16] and [S19] provide no information as to whether cells can approach the steady state when antibiotic concentrations are transiently perturbed. However, we can address this kinetic question qualitatively by implementing a quasi-steady-state approximation in which the effect of drug on cell growth (Eq. [S19]) and the

growth-rate dependence of enzyme levels (Eq. [S13]) remain satisfied as internal antibiotic concentration changes. In this limit we write the rate of change of the internal concentration a_i as

$$\frac{da_i}{dt} = \kappa \cdot \left(a_e - a_i \cdot \left(1 + \rho \frac{1}{1+a_i} \frac{1}{1+\sigma \cdot a_i} \right) \right) \equiv f(a_i) \quad [\text{S44}]$$

This form is dictated by the effects of drug influx and efflux (or modification, degradation) on the internal drug concentration. Eq. [S16] gives the steady state condition of Eq. [S44], i.e., $f(a_i) = 0$.

We perform linear stability analysis with respect to changes in concentration by perturbing about the steady state solution $a_{i,s}$, defined by $f(a_{i,s}) = 0$. The expected response to small perturbations $\delta a_i = a_i - a_{i,s}$ is $\delta f = c \cdot \delta a_i$, with

$$c \equiv \left. \frac{\partial f}{\partial a_i} \right|_{f=0} = -\kappa \cdot \left. \frac{\partial}{\partial a_i} a_e(a_i; \rho, \sigma) \right|_{a_i=a_{i,s}} \quad [\text{S45}]$$

and using Eq. [S16] for the dependence of $a_{i,s}$ on a_e . Stability requires $c < 0$ such that the system returns to the steady state for small perturbations away from the stationary solution. The sign of c can be easily determined graphically, by inspecting the form of $a_e(a_i)$ as depicted in Fig. 17A-B: We see that $\partial a_e / \partial a_i < 0$ only in the intermediate (red) segment in between the two extrema. Thus, $c > 0$ and the solution $a_{i,s}$ in the intermediate range between a_i^* and a_i^\dagger is unstable, while everywhere else the solution is stable. This geometric statement can be readily proved algebraically for any values of the parameters for this system.

3. Generalizations of the model and applicability to tetracycline resistance: detailed descriptions of drug influx and efflux

In our analysis of antibiotic resistance above, we made several simplifying assumptions to describe the passive penetration of antibiotics into cells. Here we describe which assumptions may be relaxed without qualitatively changing central results described above. Doing so enables us to provide an independent estimate of the permeability parameter κ to compare with the value fixed by results in the main text (table S2). We also demonstrate the applicability of the model to more complicated antibiotic resistance systems, using efflux of tetracyclines via TetA as a second model system.

3.1 Effective membrane permeability

First we must appreciate that permeability (κ) in the sense used above depends on both the specific permeability (π) of antibiotic through the membrane, and the surface area (A) of the cell membrane such that the rate of molecules passing through the membrane is

given by

$$j_{\text{influx}} = \pi \cdot A \cdot ([a]_{\text{ext}} - [a]_{\text{int}}) \quad [\text{S46}]$$

with π in units of distance per time (lower-case j denotes flux of molecules rather than flux of concentration described by J in Fig. 3B and Eq. [S7]). One recovers

$J_{\text{influx}} = \kappa \cdot ([a]_{\text{ext}} - [a]_{\text{int}})$, the rate at which intracellular concentration increases in Eq. [S7], with the definition

$$\kappa \equiv \pi \cdot \frac{A}{\Omega}, \quad [\text{S47}]$$

taking Ω to be the volume of the cell.

3.1.1 A single effective membrane permeability can describe the combined permeability of both the inner- and outer- membranes

The simplest justification for the use of Eq. [S45] or [S7] is for antibiotics that enter the cell passively by diffusion. However, reality is more complex. Gram⁻ bacteria possess both outer- and inner-membranes, each with their own characteristic permeabilities that in general depend on the levels of porins and low affinity efflux pumps (93, 94). Despite these complexities, we show below that in many cases, including for the Cm-CAT system, Eq. [S7] or [S46] is a reasonably effective model of drug influx at steady state.

Allowing for separate permeability rates of outer and inner membranes (OM and IM), we rewrite the steady-state ($J_{\text{influx}} = J_{\text{removal}}$) as

$$0 = \kappa_{IM} \cdot ([a]_{\text{per}} - [a]_{\text{int}}) - V_0 \cdot \frac{1}{1 + [a]_{\text{int}} / I_{50}} \cdot \frac{1}{1 + K_m / [a]_{\text{int}}}, \quad [\text{S48}]$$

where $[a]_{\text{per}}$ is the concentration of antibiotic inside the periplasmic cavity and κ_{IM} is the permeability of the inner membrane. Provided that the resistance enzyme removes antibiotic from the cell completely (e.g. not merely expulsion into the periplasm), we can equate the flux of *number of molecules* across each membrane at steady state as follows,

$$j_{\text{influx}} = j_{OM} = j_{IM} \Rightarrow \pi_{OM} \cdot A_{OM} \cdot ([a]_{\text{ext}} - [a]_{\text{per}}) = \pi_{IM} \cdot A_{IM} \cdot ([a]_{\text{per}} - [a]_{\text{int}}) \quad [\text{S49}]$$

Using $j_{OM} = j_{IM}$, one eliminates $[a]_{\text{per}}$ from the above Eq. [S48] and defines an effective permeability constant

$$\tilde{\kappa} \equiv \frac{A_{IM}}{\Omega_{\text{cyt}}} \cdot \frac{\pi_{IM}}{1 + \frac{A_{IM} \cdot \pi_{IM}}{A_{OM} \cdot \pi_{OM}}} \quad [\text{S50}]$$

to recover the results of Eqs. [S15], [S16], and [S17], with $\kappa \rightarrow \tilde{\kappa}$. If the resistance mechanism in consideration expels antibiotic into periplasm, as is the case for TetA-mediated efflux of tetracyclines (88), one obtains an even simpler expression:

$$\tilde{\kappa} \equiv \kappa_{IM} = \pi_{IM} \cdot \frac{A_{IM}}{\Omega_{\text{cyt}}}, \quad [\text{S51}]$$

a result independent of outer membrane permeability at steady state. These results connect our simple permeability parameter κ to the biophysical properties of the cell and motivate our claim that antibiotic influx can be treated according to Eq. [S7]. Henceforth, we drop the tilde notation with the understanding that κ is used as a “catch-all” parameter in the sense above.

3.2 The effect of endogenous drug efflux and drug chelation on tetracycline resistance

We formulated our model with the goal of describing effects of antibiotics on bacterial growth in the presence of a single high affinity efflux- or enzyme-mediated drug resistance mechanism. But as described near Eq. [S7], cells often additionally possess low-affinity native efflux mechanisms that potentially complicate our simple description. Additionally, some antibiotics may be charged by chelators under physiological conditions, ultimately affecting permeation rate and equilibrium distributions of the drug across cell membranes (85). We briefly treat the effects of endogenous efflux and chelation here, emphasizing that key results do not differ qualitatively from those derived above.

3.2.1 Modeling drug influx in the presence of endogenous drug efflux and drug chelation

We begin by incorporating the effects of chelation or endogenous efflux into our description of passive influx of drug into the cell. We assume the presence of low-affinity efflux or chelation alters the equilibrium concentration of internal drug by a factor of η such that $[a]_{\text{int}} = \eta \cdot [a]_{\text{ext}}$ at equilibrium. When η characterizes low-affinity efflux, comparison with Eq. [S9] reveals that $\eta \equiv \left(1 + V_{\text{native}}^{\text{max}} / \kappa \cdot K_{\text{native}}\right)^{-1}$, and $\eta \leq 1$. If the parameter characterizes chelation, then η may take any positive value, indicating that Donnan potential may act to either increase ($\eta > 1$) or decrease ($\eta < 1$) internal drug concentration relative to extracellular concentration. One can thus describe the influx by modifying Eq. [S7] to the form

$$J_{\text{influx}} = \kappa \cdot ([a]_{\text{ext}} - [a]_{\text{int}} / \eta). \quad [\text{S52}]$$

Yet another layer of detail is that equilibrium may be shifted (as described above) separately across the inner and outer membranes, giving two shift factors: η_{per} and η_{cyt} . For example, an endogenous efflux pump could expel antibiotic from the cytoplasm into the periplasm (described by η_{cyt}), and this would have no effect on the equilibrium distribution of the drug between the periplasm and external medium (described by η_{per}).

3.2.2 Effects of endogenous drug efflux and drug chelation on phase coexistence,

MIC, and MCC

Without providing the algebraic details here, we affirm that one can recover the steady state relation Eq. [S16] by balancing influx across cell membranes with a high-affinity efflux term J_{removal} , and then rescaling variables judiciously. All subsequent derivations proceed as before, and one can show that in analogy to Eq. [S21],

$$\rho_c(\sigma, \eta_{\text{per}} \cdot \eta_{\text{cyt}}) = \frac{(\sigma^{-1/3} + 1 + \sigma^{1/3})^3}{\eta_{\text{per}} \cdot \eta_{\text{cyt}}} \quad [\text{S53}]$$

And in place of Eq. [S28] we have

$$\text{MIC} \approx \frac{V_0 / \kappa_\eta}{\left(1 + \sqrt{K_m / I_{50}}\right)^2} + \frac{\sqrt{K_m \cdot I_{50}}}{\eta_{\text{per}} \cdot \eta_{\text{cyt}}} + \dots \quad [\text{S54}]$$

with high-affinity efflux described by V_0 as before, and κ_η as effective permeability that generally depends on η_{per} and η_{cyt} . We showed above that effective permeability κ is defined by flux balance and depends on details of efflux (Eqs. [S50], [S51]) and κ_η must be defined in the same manner. The essential qualitative results of the model have not changed; though this analysis shows that, for example, endogenous low-affinity efflux ($0 < \eta < 1$) would shift the critical point to a higher value (delaying the onset of bistability), but would not affect the linear relation between MIC and V_0 . And in analogy to Eq. [S40], the theoretical MCC is given

$$\text{MCC} \approx 2 \cdot \left(\sqrt{K_m} + \sqrt{I_{50}} \right) \cdot \sqrt{\frac{\text{MIC}}{\eta_{\text{cyt}} \cdot \eta_{\text{per}}}} \quad [\text{S55}]$$

Chloramphenicol is electrically uncharged at physiological pH and believed to move passively across the cell membranes (41), and we can regard $\eta_{\text{per}} \approx \eta_{\text{cyt}} \approx 1$.

3.2.3 Modeling tetracycline efflux by TetA in the presence of Tc-chelation

Tc is chelated by Mg^{2+} ions that strongly affect its partition, with $\eta_{\text{cyt}} \approx \eta_{\text{per}} \approx 2$. The equilibrium cytoplasmic tetracycline concentration is thus four-fold higher than the external concentration (88). In spite of this effect, we are justified in determining V_0/κ_{Tc} using Eq. [S28] rather than Eq. [S54] (table S5), because with $\text{MIC} \approx 700 \mu\text{M}$ (fig. S11A) and $\sqrt{K_m \cdot I_{50}} \approx 6.5 \mu\text{M}$ (table S5), we have $\text{MIC} \gg \sqrt{K_m \cdot I_{50}}$ and Eq. [S54] is essentially equivalent to Eq. [S28] with the definition $\kappa_{\text{Tc}} \equiv \kappa \cdot \eta_{\text{per}}$ (for TetA efflux, flux balance analysis reveals $\kappa_\eta = \eta_{\text{per}} \cdot \kappa$, independent of η_{cyt}).

Because $\eta_{\text{cyt}} \approx \eta_{\text{per}} \approx 2$ for Tc, Eq. [S55] predicts MCC values for the drug-resistant strain Ta1 to be lower (relative to MIC) than that predicted by Eq. [S40]. However, high levels of Tc (and other antibiotics) have been shown to depolarize cell membranes (95, 96), so

the shift factors likely have growth rate-dependence for which $\eta \rightarrow 1$ when Tc concentrations are high enough to completely inhibit growth. Thus, MCC in these systems may take some intermediate value between that given by Eq. [S40] and that by Eq. [S55]. Nonetheless, the plots in fig. S11A-B depict the region of bistability predicted by the analysis above with $\eta_{\text{cyt}} = \eta_{\text{per}} = 2$ for all antibiotic concentrations.

3.3 Independent estimates of the cell's permeability to chloramphenicol

To determine whether our prediction of $\kappa \sim 1.5 \text{ s}^{-1}$ for chloramphenicol (based on MIC and CAT activity of Cat1, table S2) is reasonable, we estimate here the specific permeability of *E. coli*'s inner- and outer-membranes (IM, OM) to Cm using primarily the method outlined by Thanassi *et al.* (88), which is based on Cm hydrophobicity, charge, etc. Then we compose an effective permeability constant from the specific permeabilities with Eq. [S50].

3.3.1 Inner membrane permeability

Collander (97) demonstrated that a molecule's specific permeability π through a typical lipid bilayer membrane (similar in composition to the inner membrane in *E. coli*) is related to the molecular weight (MW) and the partition coefficient c of the molecule in ether-water such that $\log(c^{1.3}) \sim \log(\pi \cdot MW^{1.5})$ at 20°C. The apparent partition coefficient of Cm in ether-water for $2.0 \leq \text{pH} \leq 9.0$ is given (98) at 25°C as $c_{25}=3$. However, to use Collander's relation and obtain permeability, we must correct for the temperature dependence of partition coefficients (99) $\pi(T) \propto e^{-E_a/RT}$. We take Pramer's (100) value of activation energy $E_a \sim 10^4$ cal/mol, based on the diffusion of Cm into *Nitella* cytoplasm; this number is comparable to values for other antibiotics passing solely through lipid bilayer (88, 99). This correction gives $c_{20} \approx 2.2$. Collander's data then suggest that for molecules with MW and partition coefficient similar to those of Cm, the permeability falls in the range $10^{-5} \leq \pi \leq 10^{-4}$ cm/s. To obtain the specific permeability at 37°C, we again correct for temperature to obtain

$$2.6 \times 10^{-5} \lesssim \pi_{I.M.} \lesssim 2.6 \times 10^{-4} \text{ cm/s} . \quad [\text{S56}]$$

3.3.2 Outer membrane permeability

Estimating outer membrane permeability is less direct and we must appeal to permeabilities of other compounds. Chloramphenicol diffusion through OM porins is much faster than through lipopolysaccharide, and loss of porin production significantly decreases the ability of Cm to inhibit growth (93, 101). Cm diffuses through PhoE, OmpC, and OmpF porins; molecular weight, charge, size, and hydrophobicity have all been found to influence the permeability of antibiotics through these OM porins (93, 101). For the lack of direct data on chloramphenicol permeability, we use the permeabilities of two drugs with similar size and total charge (tetracycline and cephalixin) through the OmpF porin as reference points. By combining the data due to Nikaido *et al.* (102, 103), we obtain absolute permeability rates of various compounds

through porin-containing membrane as a function of hydrophobicity, with hydrophobicity given by the logarithm of the partition coefficient in n-octanol. The partition coefficient of Cm in n-octanol is reported (104) as $c_{n\text{-oct}} = 12$. Electrically neutral compounds of similar size and hydrophobicity as Cm (like cephalixin), have permeability through OmpF of $\sim 4 \times 10^{-4}$ cm/s (103). Thanassi *et al.* (88) give a permeability of the bulkier tetracycline through these porins $\sim 10^{-5}$ cm/s. We therefore estimate $10^{-5} \leq \pi_{O.M.} \leq 10^{-4}$ cm/s for chloramphenicol.

3.3.3 Comparing model predictions with estimated permeability

Then using Eq. [S50] we combine these specific inner- and outer-membrane permeabilities and cytoplasmic volume Ω_{cyt} to compute the effective permeability for both membranes together

$$0.37 \lesssim \kappa \lesssim 7.5 \text{ s}^{-1} \quad [\text{S57}]$$

with $A_i = 105 \text{ cm}^2/\text{mg}$, $A_o = 132 \text{ cm}^2/\text{mg}$, and $\Omega_{\text{cyt}} = 0.0024 \text{ cm}^3/\text{mg}$ (all mass units are dry weight of cells) (88), although we use these parameter values only as an order of magnitude estimate, and in particular the *in vitro* upper bound may be somewhat higher. In table S2 we see that our predicted value of permeability $\kappa_{\text{Cat1}} \sim 1.5 \text{ s}^{-1}$ for strain Cat1 is within this estimated range. Similarly, with V_0 fixed for all CAT-expressing strains (Fig. 4B, bottom), the parameter fitting of all CAT-expressing strains for which growth rates were measured (colored lines, fig. S17), gives an average permeability for all strains $\kappa_{\text{all}} \sim 1.5 \pm 0.14 \text{ s}^{-1}$ (SD).

Because the estimated range for κ is based solely on physical properties like the hydrophobicity, and on permeability of cells away from steady-state growth, we offer the following caveat: In our simple model (Eq. [S15]), we did not explicitly include the effects of low-affinity native efflux and porin regulation; therefore the permeability parameter κ is an effective one including such effects. (For similar reasons, we acknowledged near Eq. [S9] that our fit value of the half-inhibition constant I_{50} might actually represent an effective \tilde{I}_{50}). Therefore, we expect this κ , representing an effective permeability of the cell at steady state (from table S2), to be lower than a value estimated on physical properties alone.

Supplementary Figures

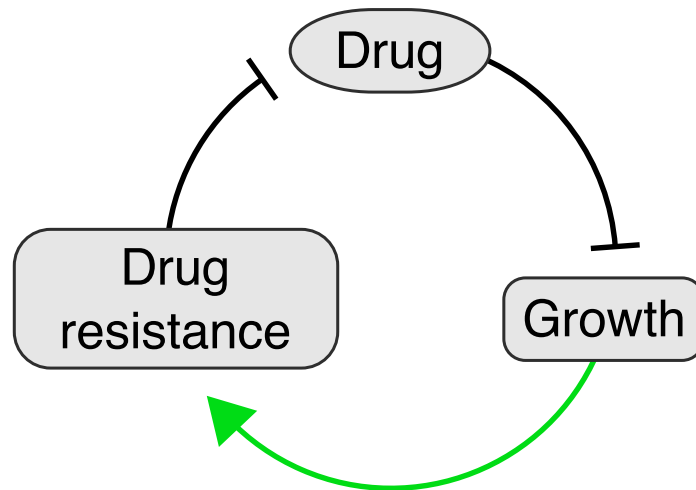


Fig. S1: Positive feedback in drug resistance.

A proposed positive feedback loop linking antibiotic drug, cell growth, and the expression of drug resistance. The positive link (green arrow) between drug-inhibited growth and gene expression is expected from global growth-mediated effects even for unregulated proteins (16).

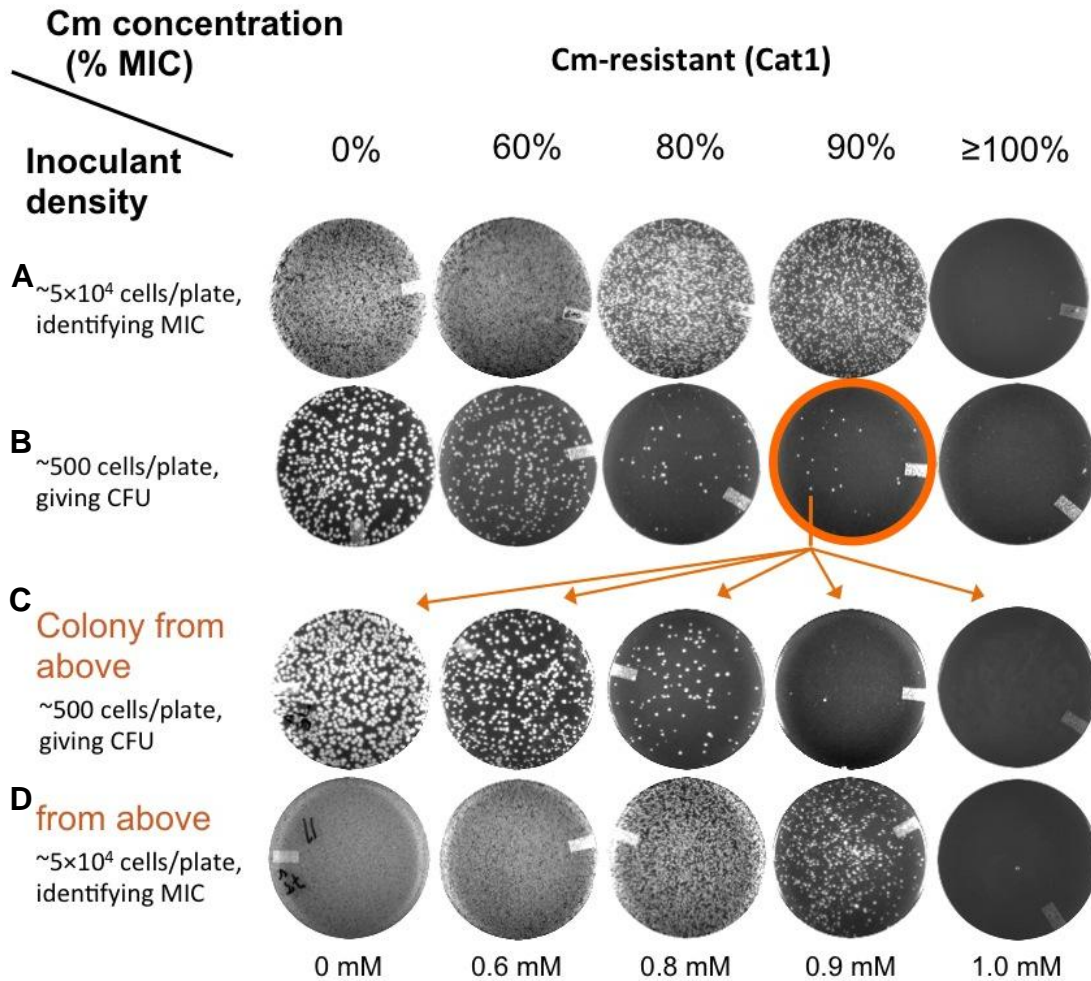


Fig. S2: The apparent MIC and viability of Cat1 cells in chloramphenicol from plate assays. Typical results for the growth of Cm-resistant (Cat1) cells on LB agar plates containing various concentrations of Cm (shown at the bottom). Cells were diluted from log phase batch cultures lacking Cm, and were spread onto agar at densities indicated on the left of each panel. Plates were incubated overnight for ~18 hours at 37°C; see Supplementary Methods for details. **A**, To determine the apparent MIC, referred to as MIC_{plate} and defined as the Cm concentration above which visible colonies formed at a fraction of less than 10⁻⁴ per inoculum after 18 hours of incubation, the plates are plated at very high densities. The plating results lead to the value of MIC_{plate} = 1.0 mM for this strain. Similar results were obtained from replicates. **B**, 100-fold lower cell density was used to reveal differential fraction of colony formation for the Cat1 strain. The number of colonies formed decreases steadily over sub-MIC Cm concentrations. The fraction of colonies formed per inoculum is plotted in Fig. 1B (green circles). **C-D**, The few Cat1 colonies that formed on plates with Cm concentration close to 80-90% of MIC_{plate} are not mutants. A colony chosen from the indicated plate (orange circle in panel **B**) was grown in the batch culture and replated on LB agar with the same range of Cm at low or high density (panels **C** and **D** respectively). The results obtained are similar to those from Cat1 cells that had never been exposed to Cm (compare panels **A** and **B**).

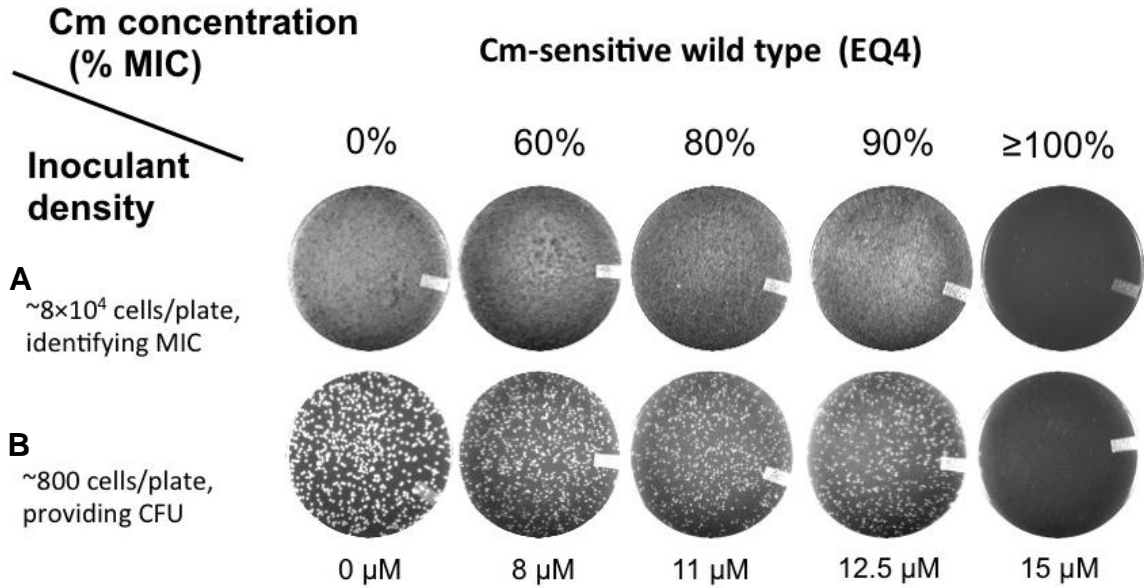


Fig. S3: The apparent MIC and viability of wild type (EQ4) cells in chloramphenicol from plate assays. Same as in fig. S2 panels **A** and **B** but for wild type cells. MIC_{plate} is determined to be 15 μM from high density plating (panel **A**). The number of colonies formed on each plate remains nearly constant as the Cm concentration approaches MIC_{plate} (panel **B**), in contrast to the decreasing CFU count in the Cm-resistant strain Cat1 at sub-MIC Cm concentrations. The fraction of colonies formed per inoculum is plotted in Fig. 1B (blue triangles).

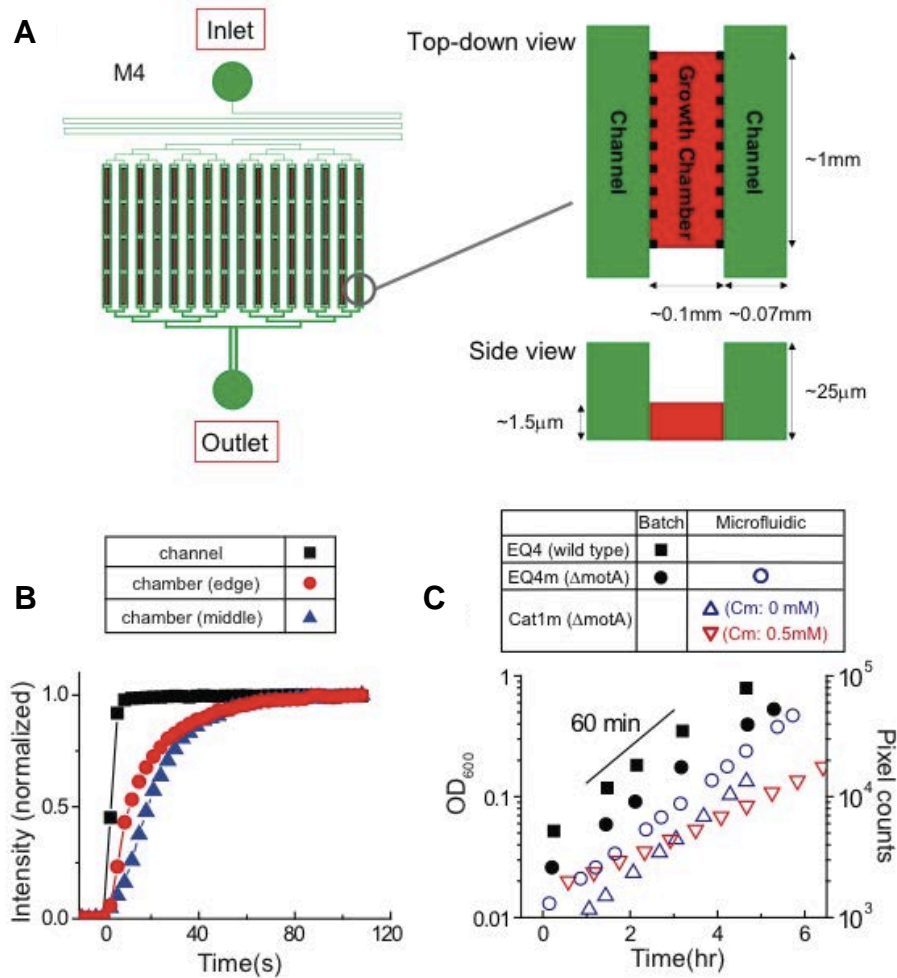


Fig. S4: Design and characterization of a microfluidic culturing device for the maintenance of Cm concentration. We designed a microfluidic culturing device to monitor cell growth in a constant environment at the single cell level. The device is similar to a previous design (28), with a few modifications. Fresh medium flows actively through the outside reservoir (channels, in green) and diffuses into the cell growth chambers (center red in top-down view, $1\text{mm} \times 0.1\text{mm} \times 1.5\mu\text{m}$). The small geometry of microfluidic chambers ensures the fast fluid exchange rate between the reservoir and the chamber. This is shown in panel **B**, where we abruptly introduced a fluorescent dye (Rhodamine 110, invitrogen) into a channel (black squares) and measured the changes in fluorescence at the edge (red circles) and in the middle (blue triangles) of the chamber. It took ~ 40 sec for fluorescence to reach 90% of its maximum level, suggesting that molecules of similar sizes as the dye are replenished approximately every 40 sec. The fast fluid exchange rate ensures that a constant chemical environment, particularly, the drug concentration, is maintained inside the chamber. This is important because the cells studied here express CAT, which modifies Cm. Thus, the Cm concentration in the growth

medium would otherwise decrease over the course of experiment, making it difficult for long-term observation.

In panel C, we compared the growth in a microfluidic chamber to that in batch culture. First of all, wild type (EQ4) cell and $\Delta motA$ (EQ4m) cells grew at similar rates in the batch culture (solid black squares and circles, respectively) and the wild type (solid black square), with ~60 min doubling time (line) in minimal medium with glycerol and NH_4^+ . Next, the growth of the $\Delta motA$ strain in the microfluidic chamber was characterized (open red circle) by counting the pixels occupied by growing colonies in phase contrast images; see Supplementary Methods). The growth rate is ~10% slower than that in batch culture.

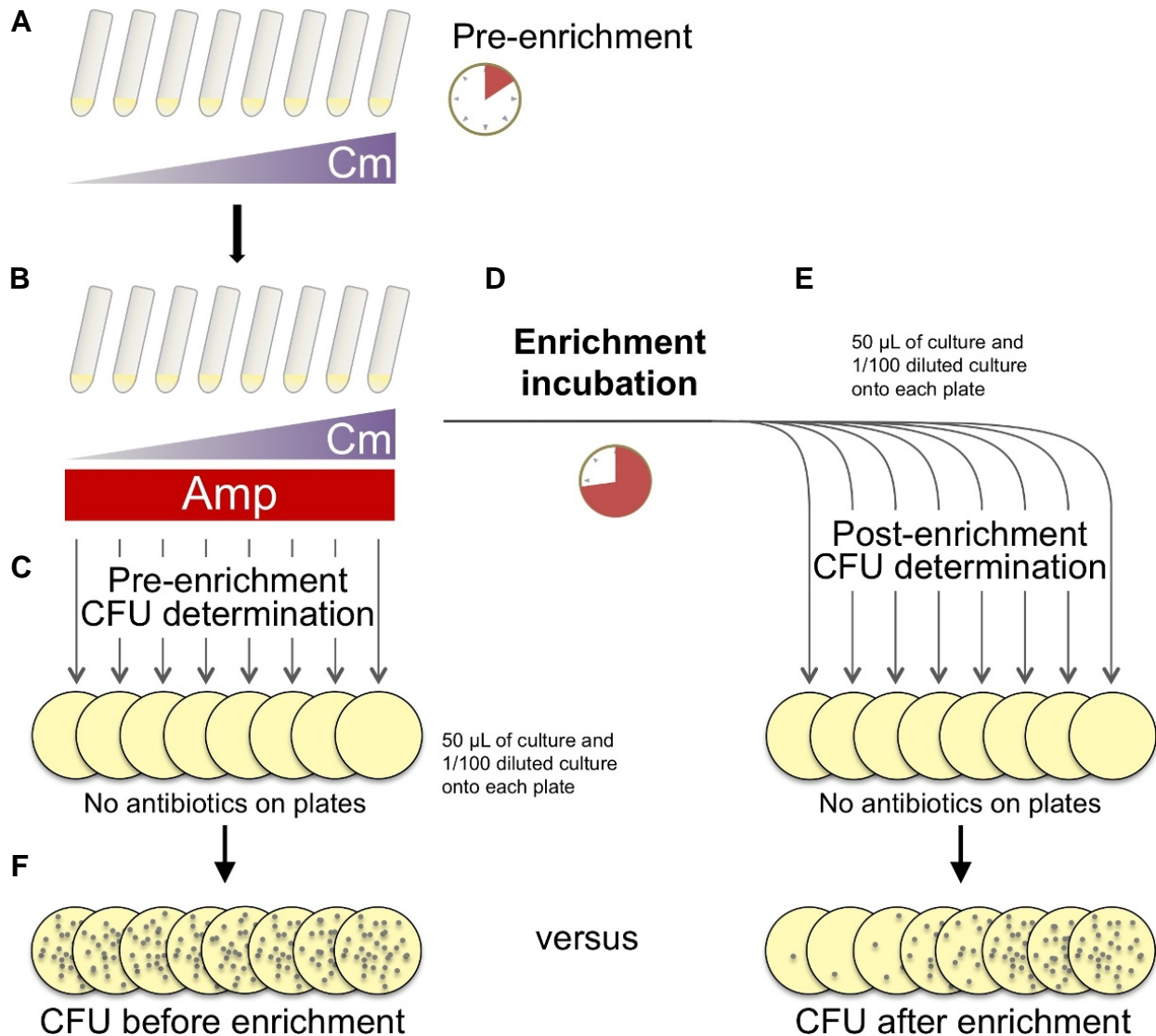


Fig. S5: Ampicillin enrichment assay. This assay takes advantage of the fact that ampicillin (Amp) kills growing cells to detect the fraction of dormant cells in a batch culture (35, 105). **A**, Batch cultures grow in glass tubes containing media with various concentrations of Cm for 1-2 hours to allow cells to acclimate to Cm upshift (from Cm-free preculture). **B**, Cultures are diluted into identical medium with Cm, together with Amp (100 $\mu\text{g}/\text{ml}$). **C**, A small volume of culture from each tube is spread onto LB plates lacking antibiotics to determine CFU per culture volume prior to enrichment (the same is done at 100-fold dilution to ensure a countable number of cells). **D**, Cultures incubate in the amp-enriched media for 6-7 hours. During this incubation period, cultures become enriched for dormant cells as ampicillin kills growing cells rapidly but has little effect on non-growing cells (35). **E**, Identical volumes of cells from each post-enrichment culture are spread onto LB-agar plates lacking antibiotics. **F**, Plates incubate overnight at 37°C to

reveal colonies formed from cells that remained dormant during enrichment. Comparisons between post- and pre-enrichment CFU yields the fraction of dormant cells in each culture, plotted in Fig. 2F for strain Cat1. See also fig. S7.

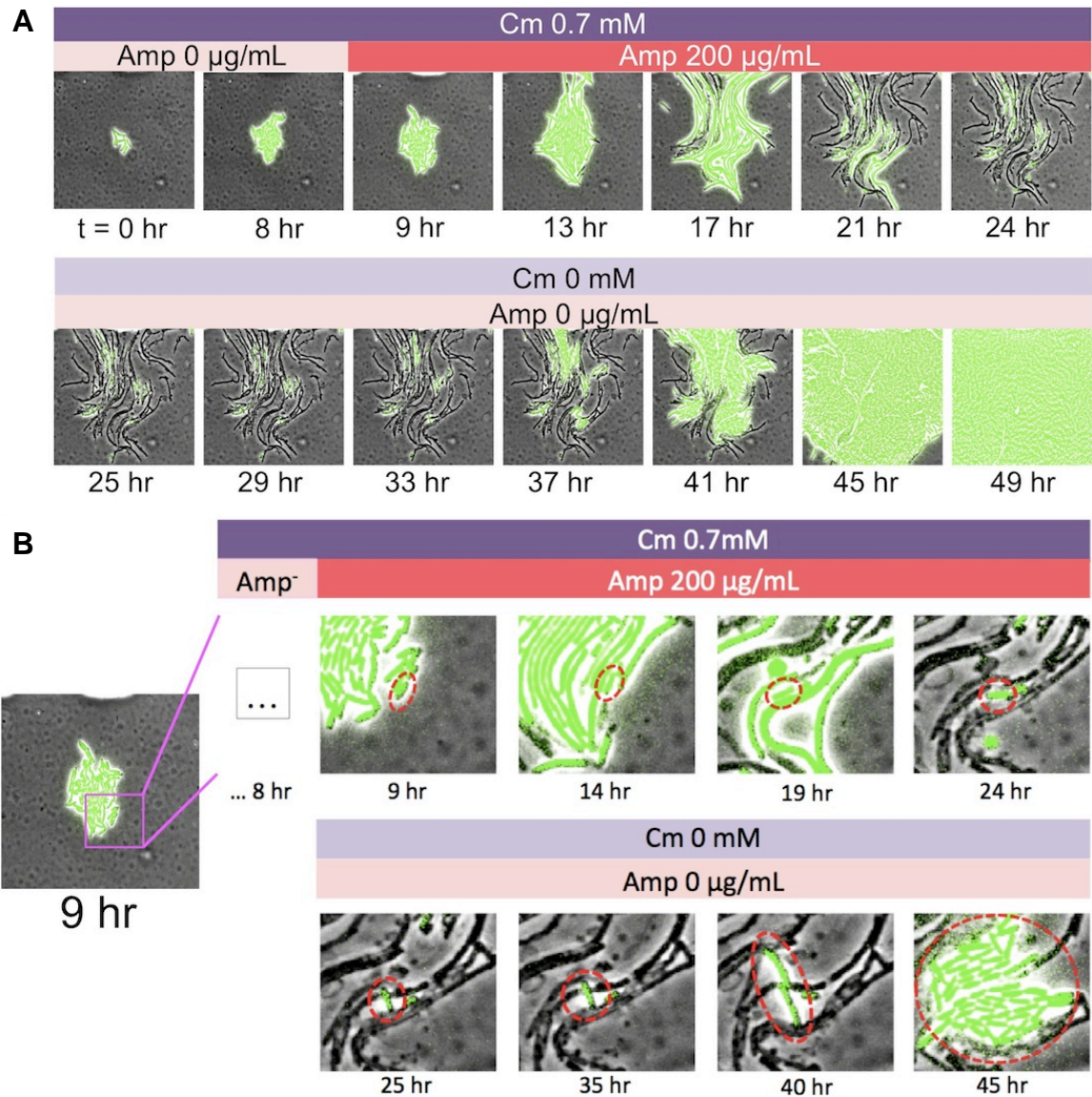


Fig. S6: Ampicillin enrichment in microfluidic chambers. **A**, This assay was performed in the microfluidic chambers for GFP-expressing Cat1m cells (Gcat1m) growing in minimal medium. We introduced 0.7 mM Cm into the medium at time zero, and added Amp (200 $\mu\text{g}/\text{ml}$) at $t=9$ hr. By $t=24$ hr, most cells appeared elongated, stopped dividing, and lost fluorescence (characteristic of the loss of cytoplasmic contents accompanying cell lysis and death (106)). After switching to drug-free medium at $t=25$ hr, cells with fluorescence (those that were not killed by Amp) began growing again, becoming clearly visible after a 12-hr wait ($t=37$ hr). **B**, Detail of (A) shows that only dormant cells survive ampicillin treatment. The history of microcolonies was tracked backwards in time, throughout and prior to enrichment. The red circle shows the history of a representative dormant cell after ampicillin was added at $t=9$ hrs. By visual inspection, we observed that this cell was not growing before and after ampicillin addition at $t=9$ hrs, but began growing after we removed Amp and Cm. Using this technique we found that cells

surviving enrichment (and subsequently creating new microcolonies at $t=25$ hr) were always dormant prior to enrichment, with no colonies forming from cells growing during Cm or Amp+Cm treatment.

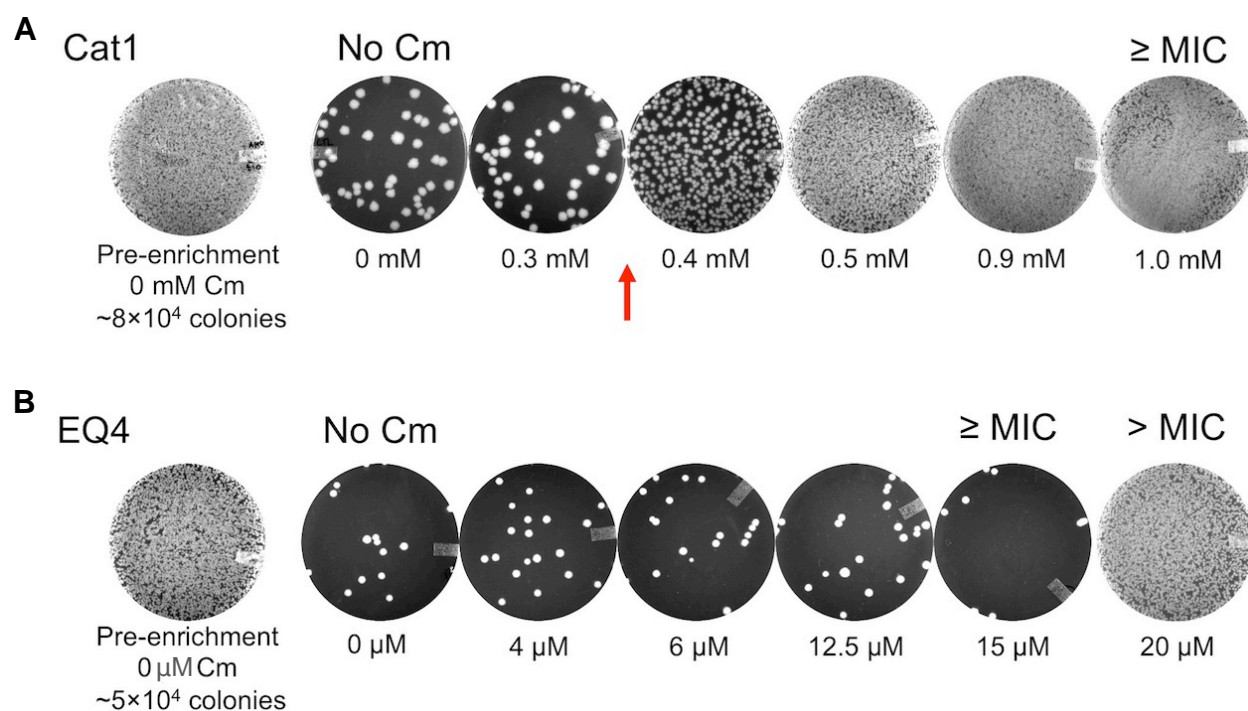


Fig. S7: The MCC of Cat1 and wild type cells. Cat1 and wild type (EQ4) cells were treated by the Ampicillin enrichment assay described in fig. S5. We measured viable cell densities of $\sim 10^3$ cells per μ L culture with dilution plating prior to enrichment (giving $\sim 5-8 \times 10^4$ colonies/plate, representative results on left). Comparisons between post- and pre-enrichment CFU yields the fraction of dormant cells in each culture. The concentrations of Cm used during enrichment are indicated beneath plates. **A**, The dormancy frequency is high at and above MIC (≥ 1.0 mM) as expected for Cm-inhibited cells (37). In the absence of Cm, we observed typical “background” dormancy frequencies of $\sim 10^{-3}$ in Amp-cultures as have been reported by others under similar conditions, attributed to the naturally occurring persisters (31, 32, 107, 108). Strikingly, colonies significantly (> 10 -fold) above the background level were obtained from Amp-treated Cat1 cultures, when enriched with concentrations of Cm well below the MIC, e.g., at 0.4 mM Cm. The ‘minimal dormancy concentration’ (MCC), defined as the minimum Cm concentration above which at least 1% of the inoculant survives enrichment, is found to be between 0.3-0.4 mM for this strain (red arrow). A conservative cutoff of 1% is used here to avoid false positives due to variability (108) in the naturally appearing persisters (31, 32, 107) and possible variability in culture density. **B**, Wild-type cells could not survive ampicillin treatment even with Cm concentrations close to the MIC, e.g., for very slowly growing cultures with $\lambda \lesssim 0.15 \text{ hr}^{-1}$ at $[\text{Cm}]_{\text{ext}} > 12 \mu\text{M}$ (Fig. 3D). Less than 0.1% of wild-type cells formed colonies post-enrichment, for all sub-MIC Cm concentrations used during enrichment (indicated at the bottom), similar to the naturally occurring persisters in Amp enrichment without Cm (31, 32, 107, 108). The results suggest that most wild-type cells grew in sub-inhibitory Cm and were therefore killed by Amp. Only at very high Cm concentrations ($\geq 20 \mu\text{M}$) were EQ4 cells significantly protected from the bactericidal effects of Amp during incubation (plate to the far right).

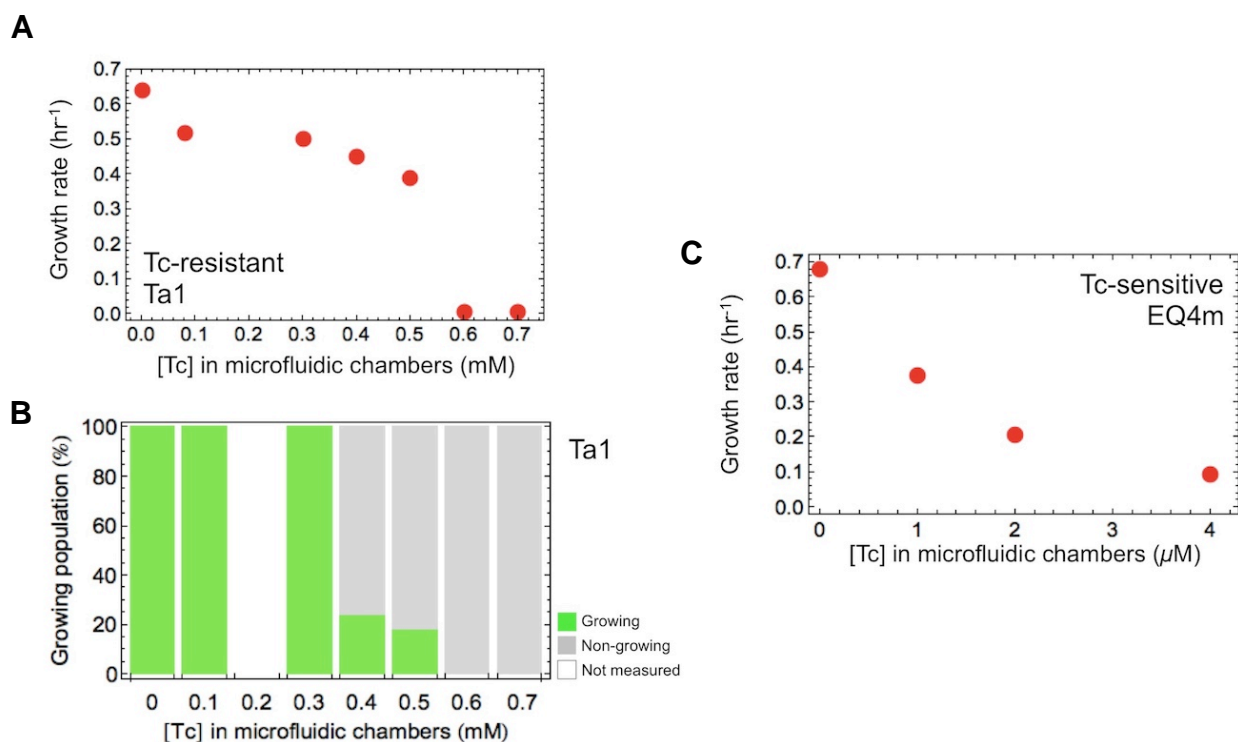


Fig. S8: Tetracycline-resistant strain Ta1 showed bimodal behavior when exposed to Tc and wild type did not. **A**, Growth rates of tetracycline-resistant strain Ta1 growing in microfluidic chambers containing minimal medium with indicated concentrations of Tc. Growth rate drops abruptly in the device at 0.6 mM Tc. **B**, Green bars give the percentage of Ta1 cells to continue growing in microfluidic chambers after adding indicated concentration of Tc (as in Figure 1E). **C**, Growth rates of wild type (EQ4m) in microfluidic device. All wild type cells grew (none were dormant) for all sub-MIC Tc concentrations. Figure S12A gives the predicted MIC, MCC, and growth rates for this strain based on growth in batch culture.

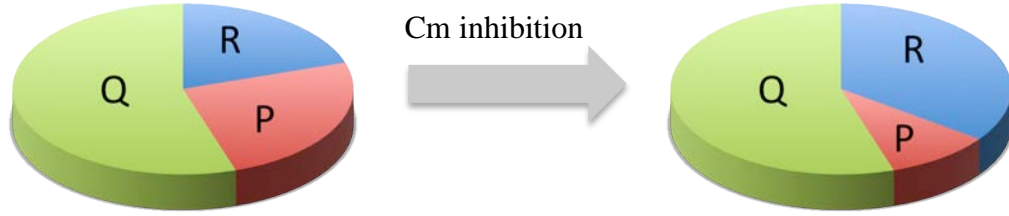


Fig. S9: Growth-mediated global effects on gene expression. The data in Fig. 3C shows that the levels of “unregulated” or “constitutively expressed” genes decrease linearly with the growth rate upon translational inhibition. The rationale of this behavior is that under translational inhibition, the cell allocates growth-limiting resources, particularly the ribosomes, to increase the synthesis of the translational apparatus (signaled by ppGpp (109)). Since most of the ribosomes are engaged in translation according to the bacterial growth laws (16), this increase results in decreased synthesis of unregulated genes. Below we summarize the basic elements of a simple mathematical model that quantitatively predicts this growth-mediated global effect on gene expression, as established by Scott *et al* (16).

The model partitions the proteome into 3-sectors (pie chart above), each governed by a distinct growth-rate dependence: (i) The ribosomal sector R, whose mass fraction ϕ_R (blue) decreases as growth is slowed down by nutrient limitation but increases as growth is slowed down by translation (as illustrated by the figure above and to be described in more detail below); (ii) a growth rate independent sector Q, whose mass fraction ϕ_Q is growth-rate independent (green); and (iii) the remaining sector P whose mass fraction ϕ_P (red) is comprised of what remains after the ribosomal sector changes in response to growth-mediated changes, i.e.,

$$\phi_P = 1 - \phi_R - \phi_Q \quad [a]$$

Constitutively expressed genes are suggested and shown to belong to the P-sector (16).

It has been known for over 50 years that exponentially growing cultures of *E. coli* exhibit an obligatory linear relation (growth law) between the ribosomal content and the growth rate λ , when growth is varied by changing nutrient composition in the medium (44, 110). In terms of the ribosomal fraction ϕ_R introduced above, this growth law can be written mathematically as

$$\lambda = \gamma \cdot (\phi_R - \phi_0) \quad [b]$$

where the proportionality constant γ is established to be the translation rate (16), and ϕ_0 is an empirically determined offset.

Scott *et al.* (16) established another linear relation between ϕ_R and λ if growth is varied by changing the translation rate γ , either by using various translational mutant or by applying sub-lethal doses of translation-inhibiting antibiotics, under a given saturating nutrient source,

$$\lambda = \nu \cdot (\phi_R^{\max} - \phi_R) . \quad [c]$$

This relation describes a trend of increase in the ribosomal fraction when growth is slowed by translational inhibition such as sub-lethal dose of Cm inhibition studied in this work. The proportionality constant ν is found to increase for nutrients of increasing quality, while ϕ_R^{\max} is a constant that represents the maximum proteome fraction allocable to the ribosomal fraction.

The value of ϕ_R^{\max} , found empirically to be ~50% for a spectrum of nutrient sources, is interpreted by Scott *et al.* (16) to arise from the fixed proteome fraction, ϕ_Q . Thus,

$$\phi_R^{\max} = 1 - \phi_Q . \quad [d]$$

Using Eqs. [c] and [d] in [a] immediately leads to

$$\phi_p = \lambda / \nu \quad [e]$$

for translation-inhibited growth. Eq. [e] is the basis of Eq. [3] in Fig. 3, i.e., the linear relation between constitutive gene expression and the growth rate. Equations [b] and [c] can be combined to obtain Eq. [S4] with $\lambda_0 \equiv \lambda(\gamma_0, \nu)$ as the growth rate of drug-free cells, and $\lambda_0^{\max} = \lambda(\gamma_0, \infty) \approx 2.85 / \text{h}$, which is the basis for the linear relation between doubling time and drug concentration.

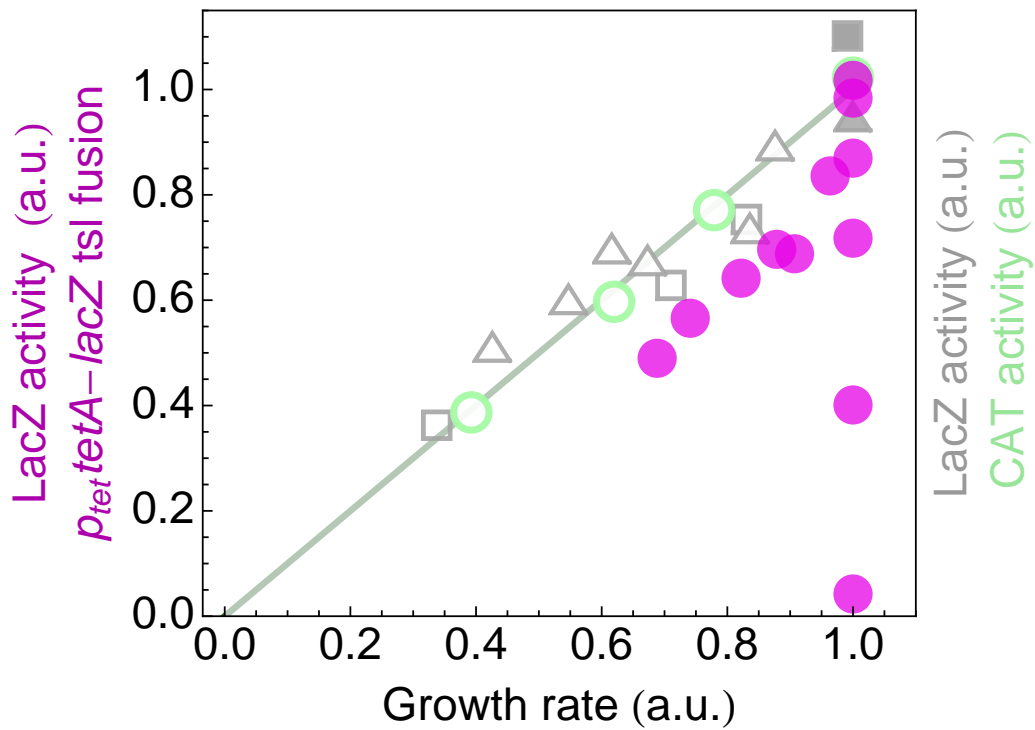


Fig. S10: Inducible resistance gene expression also depends on growth rate.

Tetracyclines (Tc) induce gene expression from the P_{tet} promoter that drives expression of the efflux pump, TetA. Data replotted from (III) (magenta) show how promoter activity is affected by growth rate (when inhibited by Tc) in a strain expressing a *tetA-lacZ* translational fusion gene from the native P_{tet} promoter. At very low Tc concentrations (too low to inhibit growth) beta-galactosidase activity is induced to its maximum level. However, activity decreases in cultures containing higher concentrations of Tc, yielding an apparently linear dependence between growth rate and gene expression that is similar to the trend observed for constitutively expressed genes (background symbols rescaled and replotted from Fig. 3C).

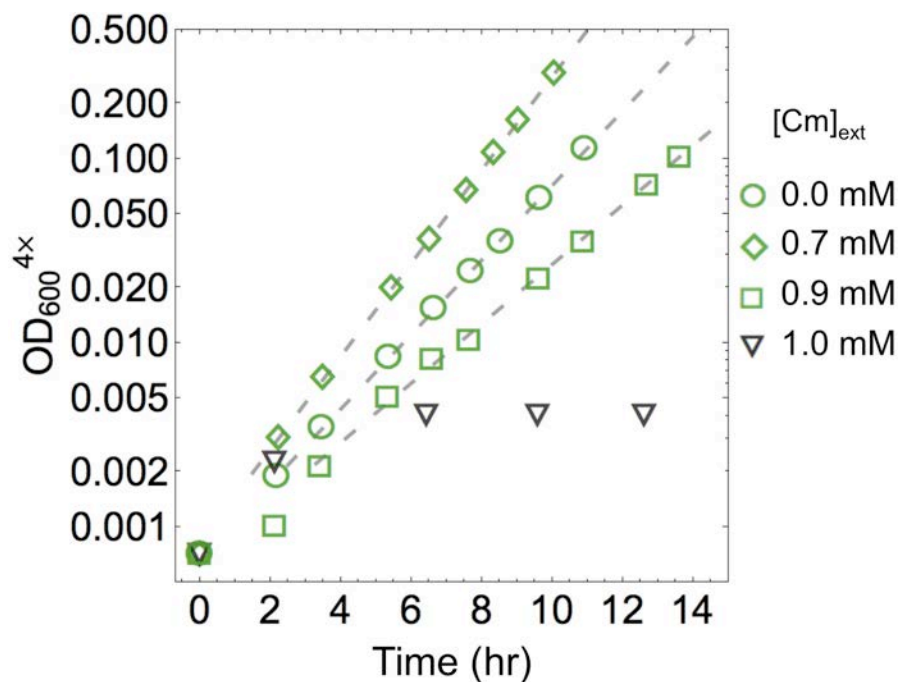


Fig. S11: Growth curves of Cat1 cells in batch culture with chloramphenicol.

Representative growth curves showing steady exponential growth in these cultures for up to seven generations, after which the experiments were usually halted. The lines are least squares fit of log-OD with time. Inverted triangles show unambiguously the non-growing cultures across the MIC.

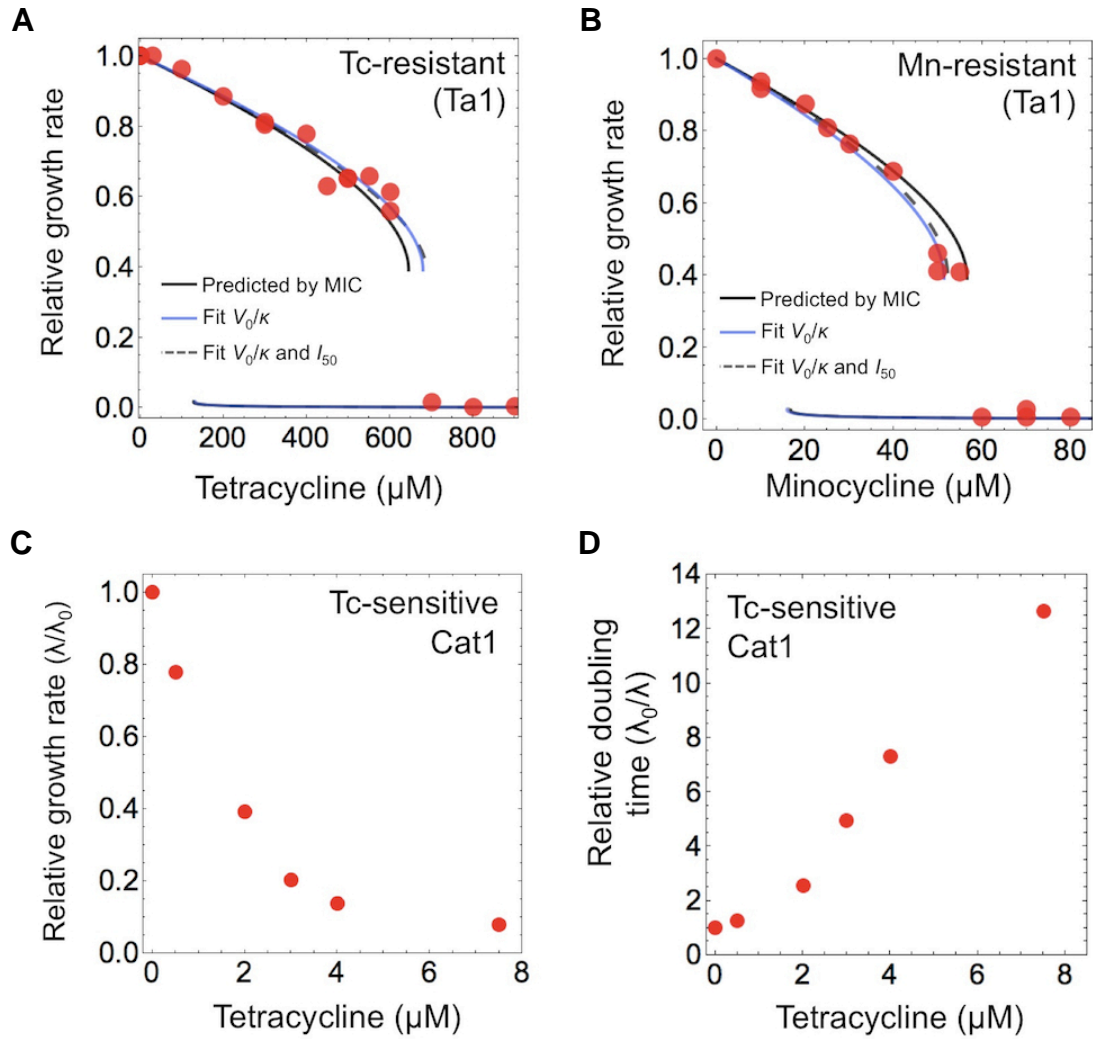


Fig. S12: The MIC and growth rates of Ta1 cells in batch culture with tetracycline and minocycline. **A**, The relative decrease in the growth rate of Ta1 cells constitutively expressing TetA in minimal medium with various Tc concentrations (red disks) is well described by the growth feedback model (various lines). The solid black line is drawn with the *in vitro* value of I_{50}^{Tc} (table S5, see also panel **D** below), and V_0/κ_{Tc} as fixed by equation [S28], with $\text{MIC}=650 \pm 50 \mu\text{M}$ from batch culture growth data (red disks). Alternatively, we fit the model to only the empirical rates of growing cultures (i.e., when $\lambda/\lambda_0 > 0.15$), fitting either V_0/κ_{Tc} alone, or V_0/κ_{Tc} and I_{50}^{Tc} simultaneously as free parameters (blue and dashed gray lines respectively). Fits using growth rates provide parameter values very close to those predicted by MIC, see table S5 for parameters and fitting procedures. All growth conditions are given in Supplementary Methods. **B**, Same as (**A**), except with minocycline instead of tetracycline. Each data point is growth rate from a single experiment, with experiments performed on three separate days. **C**, The

relative growth rates of tetracycline-sensitive *tetA*⁻ strain (Cat1) grown in minimal media with various tetracycline concentrations (red circles). In contrast to Tc-resistant strain Ta1, growth rate does not abruptly drop to near zero across some threshold tetracycline concentration. **D**, Data replotted from **(C)** shows that relative doubling time increases nearly linearly with drug concentration. Based on *in vitro* data we predict $I_{50}^{Tc} \approx 4 \mu\text{M}$ (table S5) such that doubling time should increase by a factor of two at $[\text{Tc}]_{\text{ext}} \approx 1 \mu\text{M}$ (because $[\text{Tc}]_{\text{int}} \approx 4 \cdot [\text{Tc}]_{\text{ext}}$, see discussion below Eq. [S55]). This prediction is consistent with doubling times presented here.

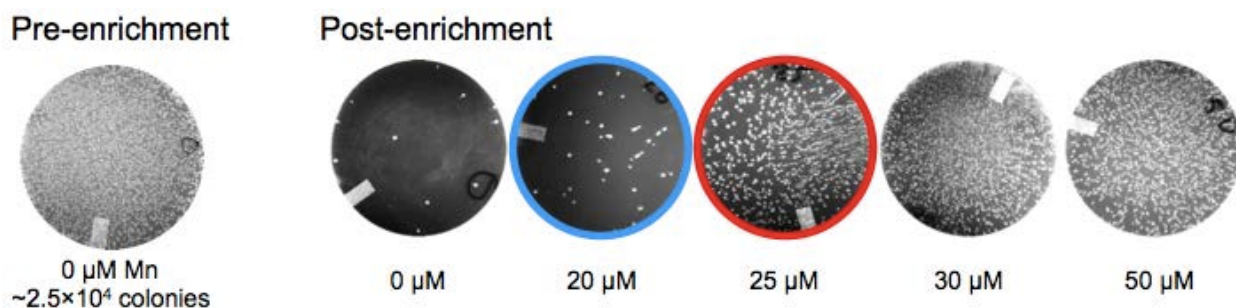


Fig. S13: Dormancy of Ta1 cells in sub-MIC concentrations of Mn. Results of batch culture Amp enrichment assay as described in fig. S5, but enriched with minocycline. Prior to enrichment incubation, cultures contained roughly 500 cells per μL as verified by control plates (50 μL culture produced $\sim 2.5 \times 10^4$ colonies/plate, see example at left). After enrichment, the same volume of culture contained fewer CFUs in cultures containing 20 μM Mn or less (due to bactericidal activity of Amp). However, above 20 μM many cells remained viable, thus revealing dormant cells below the MIC (identified as 60 μM in batch cultures in fig. S11). The MCC for TetA-Mn interaction, defined as the minimum Mn concentration above which at least 1 % of the inoculant survives enrichment, is thus between 20 and 25 μM (between red and blue circles). This is comparable to our model prediction of MCC = 15-30 μM (end of lower branch in fig. S11, the value may be as high as 30 μM as described near equation [S55] of Supplementary Discussion).

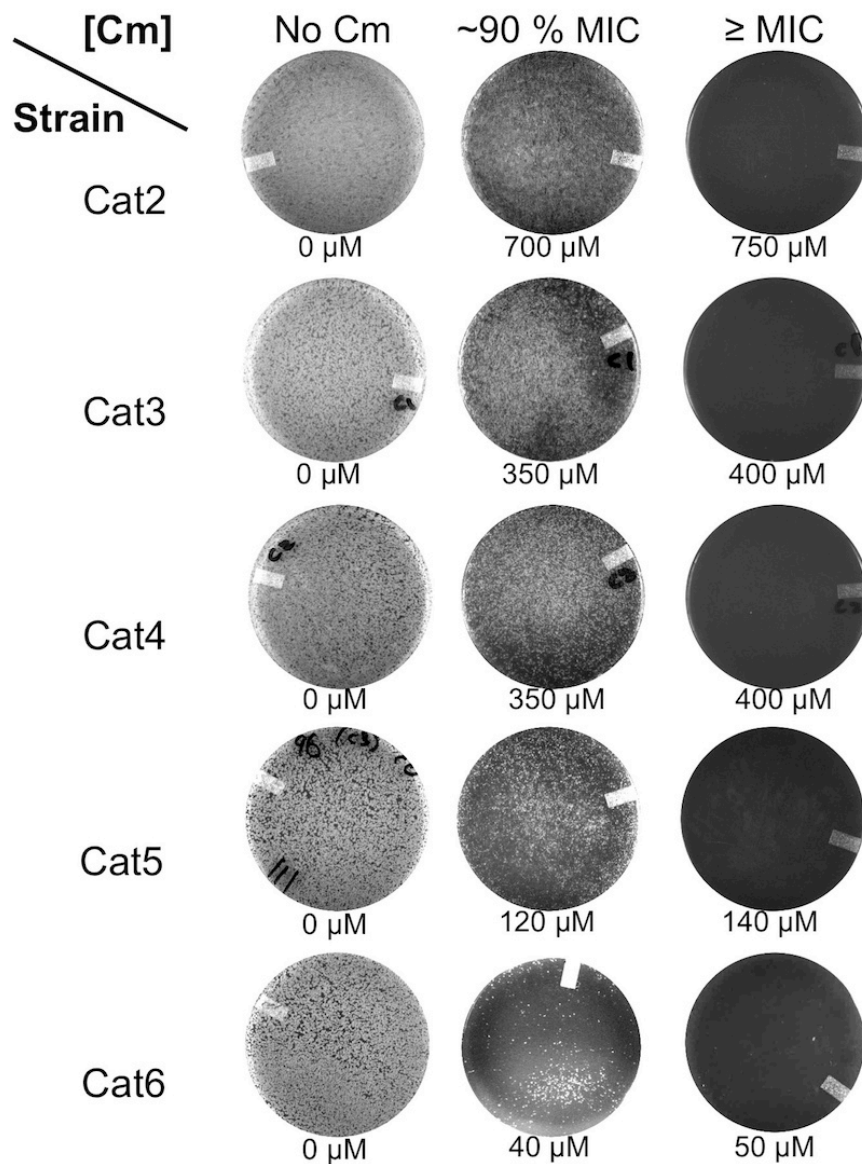


Fig. S14: Determination of MIC_{plate} for various CAT-expressing strains. These results identify MIC_{plate} values of strains Cat2 through Cat6 (table S1); they are similar to those presented in fig. S2, but each strain harbors a unique level of constitutive CAT expression. The results are intended to complement the batch culture MIC determinations used in Fig. 4. For each strain shown, cells were diluted from log phase batch cultures lacking Cm and spread onto agar plates at a density of $\sim 8 \times 10^4$ cells per plate. Plates incubated overnight at 37°C. Chloramphenicol concentrations are indicated underneath each plate, and additionally as percentage of MIC_{plate} for each strain (top row). MIC_{plate} is taken as the Cm concentration above which colonies appear at a frequency of less than

$\sim 10^{-4}$. At least two replicate experiments were performed for each strain; representative results are shown here. $\text{MIC}_{\text{plate}}$ values were similar to those obtained with batch culture growth in minimal media with chloramphenicol (it is not uncommon to find MIC of an antibiotic in LB to correspond with MIC in minimal media (43)). For the data plotted in Fig. 4B, we used only MIC data determined in batch cultures with minimal media because our model is formulated based on observations during batch culture growth (see Supplementary Discussion near equations [S5] and [S13]).

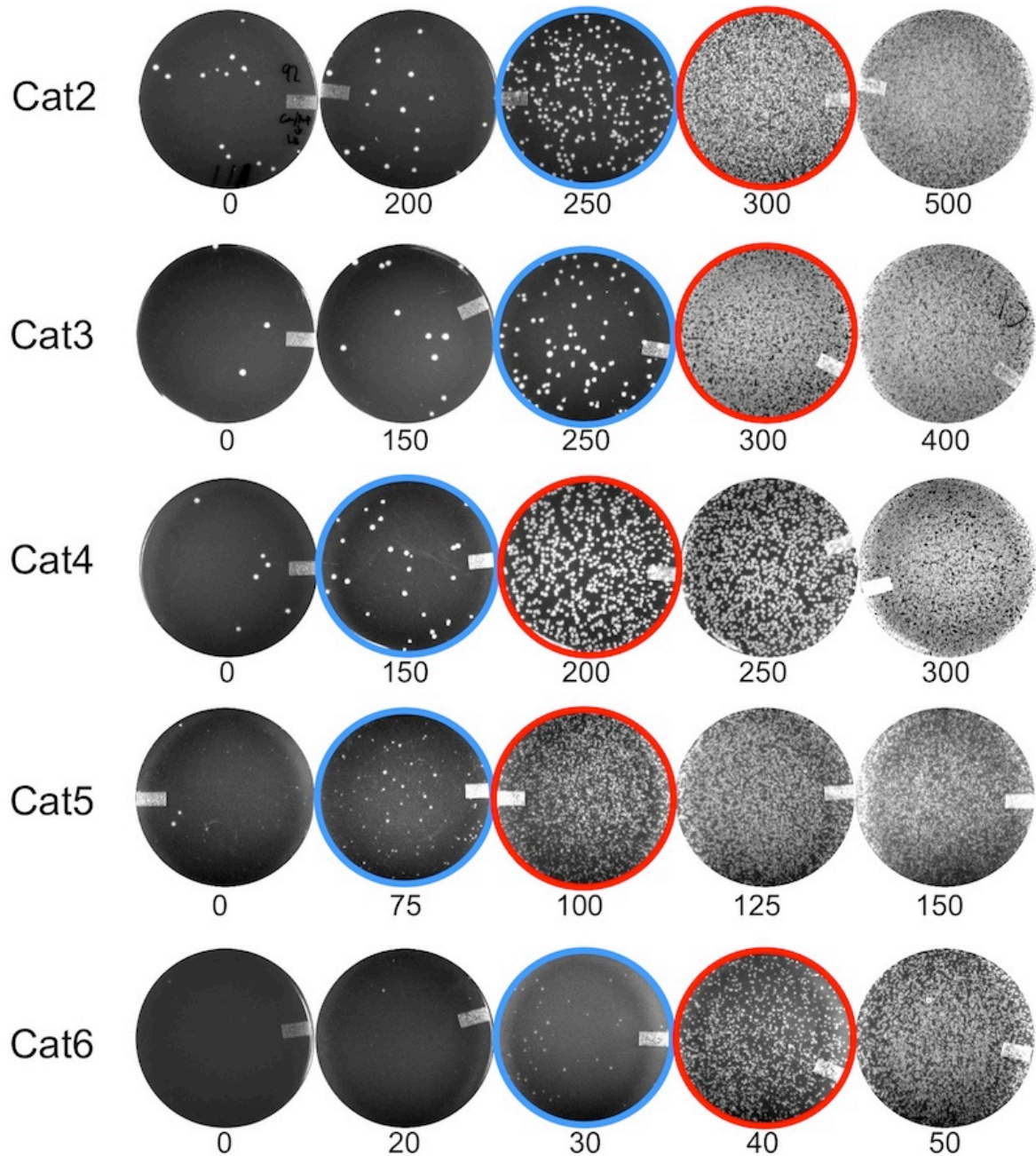


Fig. S15: Determination of MCC for various CAT-expressing strains. The Amp enrichment assay (fig. S5) was performed for CAT-expressing strains Cat2 through Cat6 to identify the MCC of each strain, representative plate results are shown here. Plates circled in red indicate that at least several percent of Amp-treated cells formed colonies, while those circled in blue indicate <1% of colony formation. The MCC value for each strain in the phase diagram of Figure 3B gives the average of at least two experiments strain (except for strain Cat4, for which we only performed the enrichment experiment once).

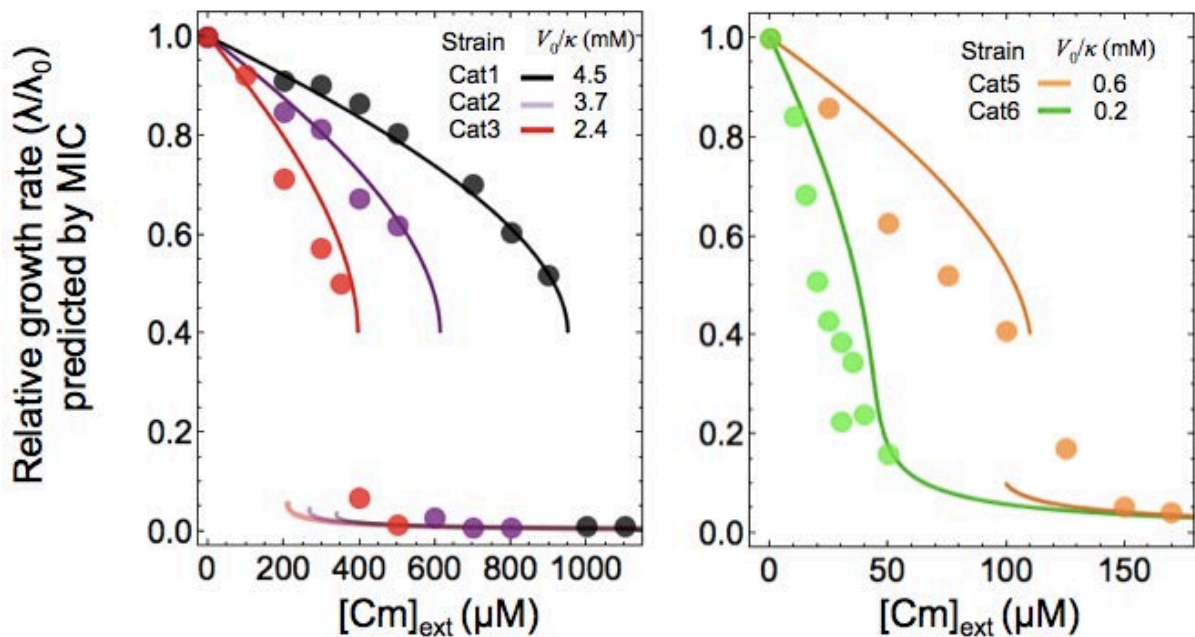


Fig. S16: Growth rates predicted by the measured MICs in the Cm-CAT system. To predict the growth rates of CAT-expressing strains in medium with various Cm concentrations (Fig. 4C-D), we used the value of V_0/κ determined by MIC for strain Cat1 together with the relative CAT activities (V_0) measured for the different strains (bottom of Fig. 4B). Here, we instead used only the empirical MICs of the CAT-expressing strains (circles in Fig. 4B) to fix the quantity V_0/κ for each strain with equation [S28]. This procedure is able to predict growth rates even if resistance enzyme activity is not easily assayable, e.g. in the Tc-TetA system for which the activity of drug resistance (provided by the efflux pump) is not readily assayable but for which MICs are available.

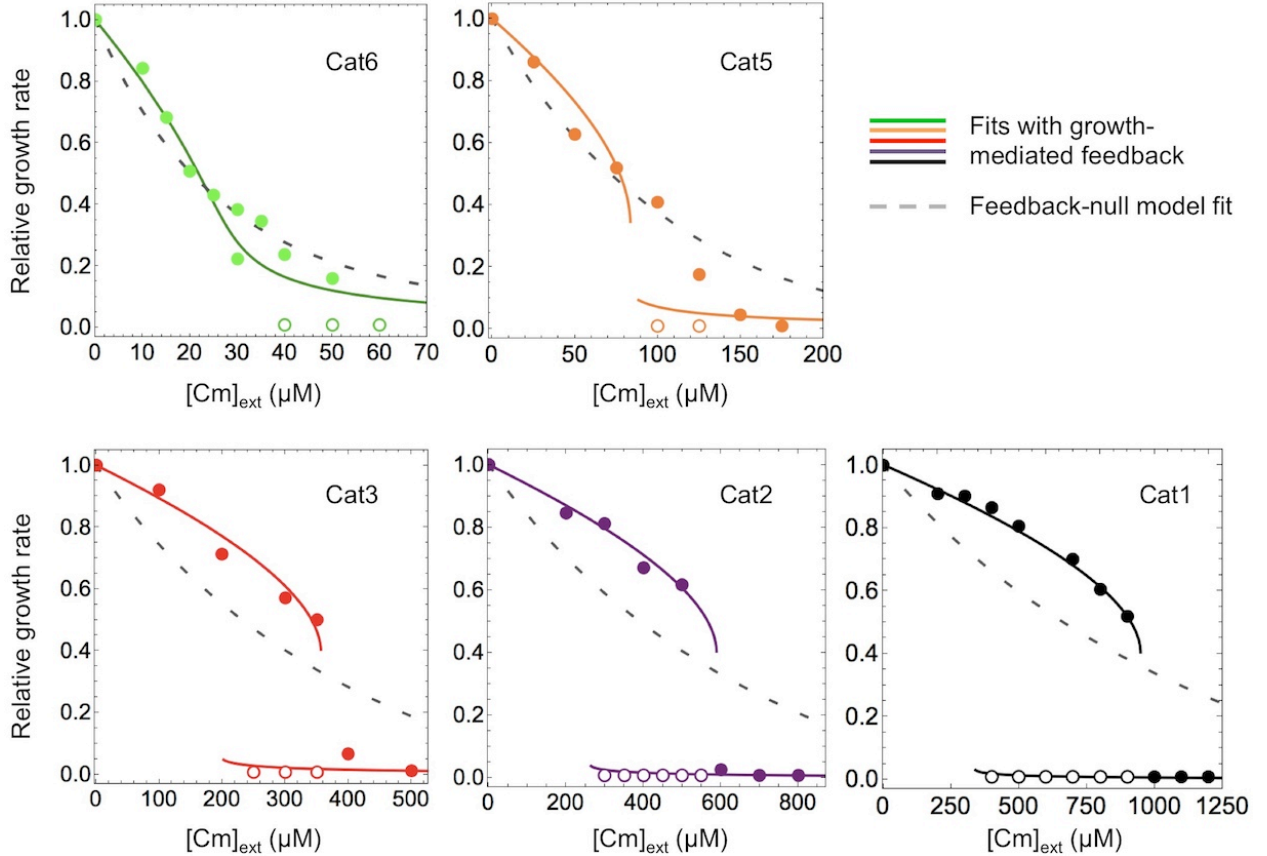


Fig. S17: Growth model without drug-induced feedback. Given the very nonlinear relation between the internal and external Cm concentrations for strongly resistant cells (Fig. 3B), we investigated whether a model without feedback, i.e., with a constant, growth-rate independent expression of CAT, might also explain the Cm-dependence of growth rate (data in Figs. 4C-3D, reproduced here as solid circles, together with Amp-enrichment data shown as open circles). The no-feedback model (Supp Discussion Eq. [S11] is used here to describe the data in this figure, using V_{\max} / κ as the only fitting parameter. The best-fit model for each strain is shown as the dashed gray line. While the no-feedback model can reasonably account for growth data of strains Cat6 and Cat5, which exhibit little or no growth bistability, the model fails to describe the growth data for the other strains that exhibit growth bistability and abrupt drops in growth rate. We fit the equation to the growth rates $\{[Cm]_{\text{ext } i}, \lambda_i / \lambda_0\}$ using the Levenberg–Marquardt method with the “NonlinearFitModel” function in Mathematica; data from slow-growing or non-growing cultures ($\lambda / \lambda_0 < 0.15$) were excluded from the fitting procedure to allow the no-feedback model the best possible chance to fit growth rates. Including the non-growing data into fits produced qualitatively similar results.

For direct comparison between presence and absence of feedback, we include a similar fit for the growth feedback model using V_0 / κ as the lone fitting parameter (solid

colored lines), again excluding the non-growing cultures from the fit procedure; the latter clearly account for the data as a whole much better. The function used to fit the data was the implicit solution to equations [1]-[3]: $\lambda / \lambda_0([Cm]_{\text{ext}}; V_0 / \kappa)$, with other parameters fixed (K_m and I_{50} , table S2). (These lines differ from the solid lines in Fig. 4C-D because the latter are not fits; they are predictions of the model using the value of V_0 / κ determined, respectively, from the measured MIC of Cat1 and the relative CAT activities of strains Cat2 through Cat6. Here we show the converse: that growth rates predict MIC reasonably well, despite the exclusion of non-growing cultures from the fitting procedure. This prediction is most striking for the strains with greatest CAT expression, in which growth rates accurately predict the location and approximate magnitude of the abrupt drop in growth. See also fig. S16).

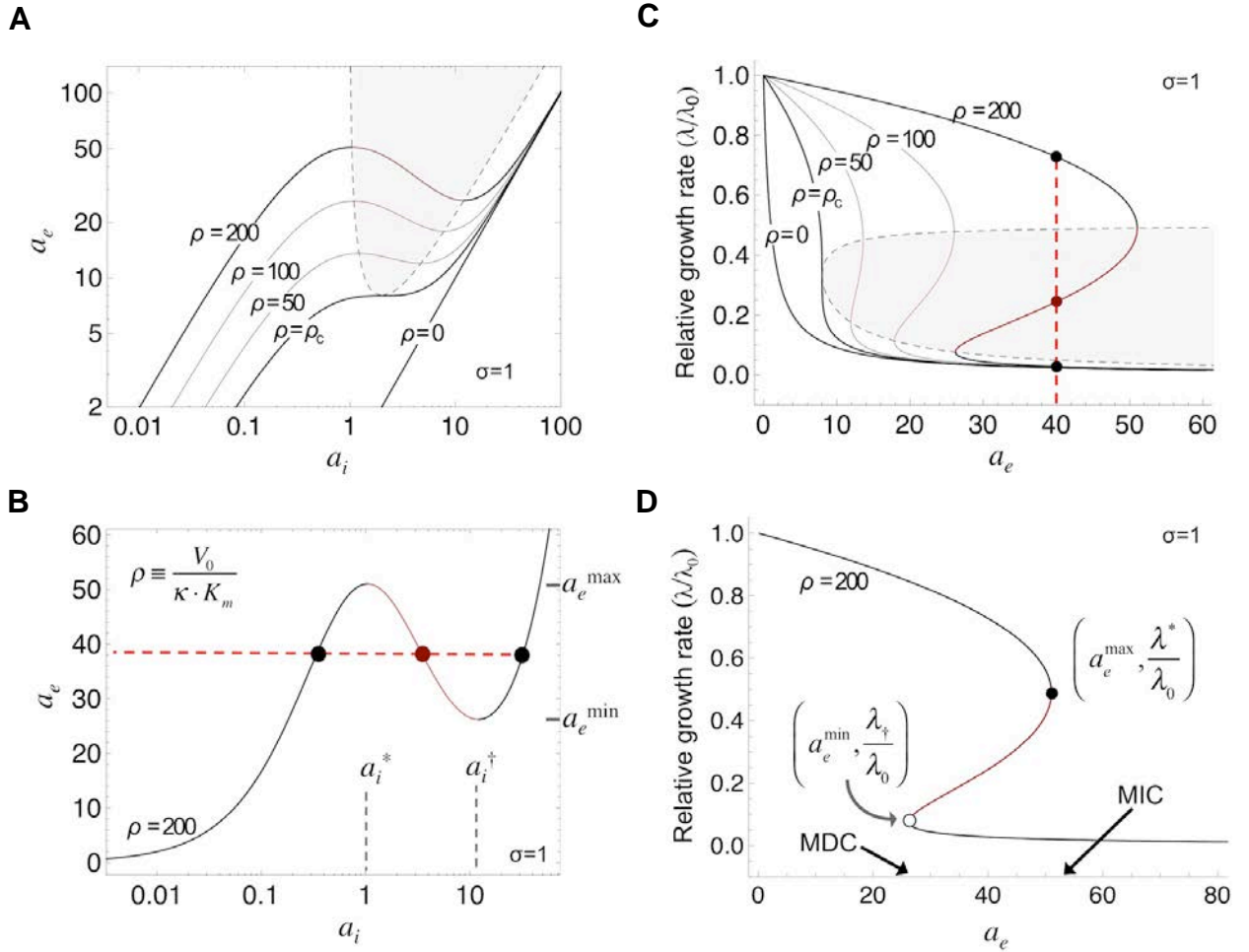


Fig. S18: Growth bistability predicted by the growth-mediated feedback model for antibiotic resistance. Model predictions for the dependence of the growth rate (λ) and the intracellular antibiotic concentration ($[a]_{\text{int}}$) on the external antibiotic concentration ($[a]_{\text{ext}}$) at steady state. The concentrations are plotted in units of I_{50} , i.e., $a_i = [a]_{\text{int}} / I_{50}$ and $a_e = [a]_{\text{ext}} / I_{50}$. There are two dimensionless parameters: $\rho = V_{\text{max}} / (\kappa K_m)$ is the *resistance efficacy* and $\sigma = I_{50} / K_m$ is the *saturability* (see Eqs. [S17] and [S18]). Saturability is of the order 1 for both Cm and Tc studied in this work (tables S2, S5), i.e. $K_m \sim I_{50}$ such that the enzyme activity approaches V_{max} prior to complete growth inhibition. For simplicity, we use $\sigma = 1$ for all plots shown here. **A**, The theoretical relation between a_i and a_e in our model is shown for a range of resistance efficacies ($0 \leq \rho \leq 200$) to give a sense of scale of this parameter. The family of curves show the region with multiple solutions (i.e., 3 values of a_i for the same a_e) for $\rho > \rho_c$, where $\rho_c = 27$ for $\sigma = 1$ according to Eq. [S21]. **B**, The same relation is shown for a strain with high resistance efficacy ($\rho = 200$). The red dashed line shows that a single extracellular concentration may map to three intracellular concentrations in the region between a_e^{\min} and a_e^{\max} . However, only two are predicted to

be stable solutions; intermediate internal antibiotic concentrations (red segments throughout the figure) are kinetically unstable (Supplementary Discussion near Eq. [S42]). The intracellular concentrations corresponding to a_e^{\min} and a_e^{\max} are a_i^\dagger and a_i^* , respectively. **C**, Plots of the growth rate (relative to the drug-free case, λ_0) as a function of a_e for various values of resistance efficacy, ρ . Note that solutions for the growth rate in the grey region are predicted to be kinetically unstable and, therefore, unobservable in experiments (red segments). **D**, Relative growth rate as a function of external antibiotic concentration for $\rho = 200$. The growth rate at a_e^{\min} and a_e^{\max} are denoted as λ_\dagger and λ^* , respectively (empty and filled circles); see Eqs. [S28] and [S39]. a_e^{\max} is identified as MIC and a_e^{\min} as MCC.

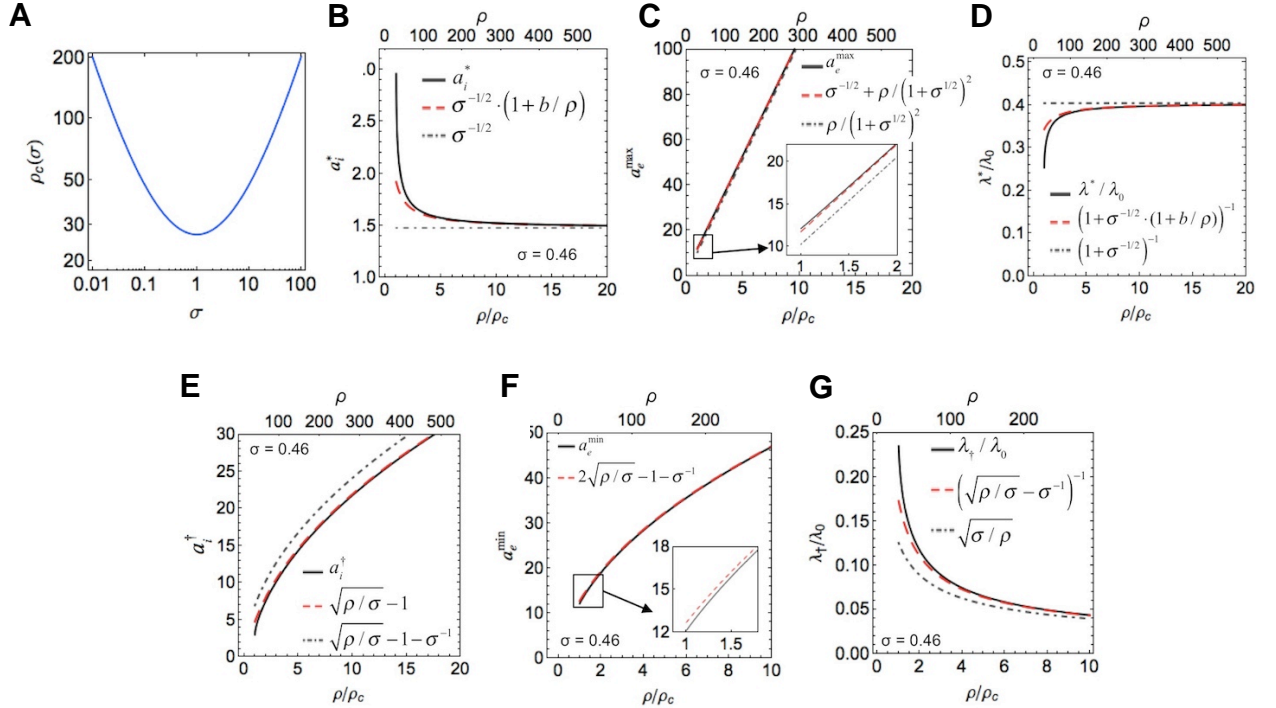


Fig. S19: Key predictions from the model and approximations in the limit of “strong”

resistance. Here we illustrate key predictions relating experimentally observable quantities to biochemical parameters in the model, revealing how observables depend on strength of resistance (see Supplementary Discussion surrounding Eqs. [S16]-[S36]). **A**, The critical resistance efficacy $\rho_c(\sigma)$ gives the minimal resistance efficacy required ($\rho > \rho_c(\sigma)$) in order for a strain to exhibit bistability over any range of drug concentrations. Quantities (**B-E**) are given for the Cm-CAT resistance system with saturability parameter $\sigma = I_{50}/K_m \approx 0.46$, see table S2 for details. **B**, The predicted internal antibiotic concentration a_i^* for cells growing in antibiotic medium just below the MIC, expressed as a function of resistance efficacy in absolute dimensionless units (top axis), or in units of critical resistance efficacy $\rho_c(\sigma)$. It is obtained as the ArgMax of equation [S16] in the supplement. **C**, The plot shows how a_e^{\max} varies with resistance efficacy. a_e^{\max} is the highest external antibiotic concentration to allow growth in a strain with strong resistance, such that $\text{MIC} \approx I_{50} \cdot a_e^{\max}$ and provides the upper bound for the region of bistability. **D**, The growth rate λ^* at a_e^{\max} gives the minimum growth rate achievable in sub-inhibitory concentrations (i.e. for $[a]_{\text{ext}}$ just below MIC), and its value is independent of resistance efficacy for strains with strong resistance. **E**, For a strain of efficacy ρ , the a_i^\dagger gives the minimum internal antibiotic concentration possible at steady state along the “low-growth” branch of the bistable region. It is obtained as the ArgMin of equation [S16] and increases with the square root of resistance efficacy. **F-G**, The

external antibiotic concentration for a cell with $a_i = a_i^\dagger$ is given by a_e^{\min} and provides the lower boundary of the bistable region. This quantity also gives the MCC in the appropriate limit (Eq. [S36]), i.e. when the growth rate at this point λ_\dagger is small (given in **G**).

Supplementary Movie Legends

Supplementary Movie 1: Example of bimodal growth in a microfluidic chamber
Genetically identical Cat1m cells express the CAT protein constitutively. Prior to imaging, cells grew exponentially for two generations in the microfluidic chambers under constant flow of minimal medium lacking Cm. At time $t=0$ hr (time indicated bottom right), media flowing into the device was switched to the same medium containing 0.9 mM Cm. Two cells in the chambers are visible in the frame at $t=0$ hr; one cell continues growing and the other becomes dormant.

Supplementary Movie 2: Non-growing cells can resume growth after Cm-downshift
In the same experiment depicted in Supplementary Movie 1 (with 0.9 mM Cm in the medium), some chambers contained only non-growing cells; this movie shows a typical non-growing cell. After 24 hours incubation the Cm concentration was reduced from 0.9 mM to 0.1 mM, a concentration well above MIC of wild type cells (see fig. S3). Growth of this cell resumed ~10 hours after Cm-downshift, indicating that the cell remained viable and retained resistance throughout the treatment despite remaining dormant.

Table S1: Bacterial strains used in this study. See Supplementary Materials and Methods for details of the construction.

Strain	Genotype	Background	Comments	AKA
EQ4 “wild type”	Δ lacIZY	MG1655	<i>E. coli</i> K-12 MG1655 with the native <i>lac</i> operon removed	—
EQ4m	Δ motA	EQ4	immotile wild type strain	EQ79
Lac1	P _{Lac-O1} - <i>lacZ</i>	EQ4	constitutive expression of <i>lacZ</i> at the <i>lac</i> locus, driven by the synthetic P _{Lac-O1} promoter	EQ5
Lac2	P _{Ltet-O1} - <i>lacZ</i>	MG1655 Δ lacI, Δ galK, Δ rhyB	constitutive expression of <i>lacZ</i> at the <i>lac</i> locus, driven by the synthetic P _{Ltet-O1} promoter	EQ37 from ref. (16)
Ta1	Km ^r : <i>rrnBT</i> : P _{Lac-O1} - <i>tetA</i>	EQ4	constitutive expression of <i>tetA(B)</i> from transposon Tn10 at the <i>ycaD</i> locus	EQ93
Cat1	<i>rrnBT</i> : P _{Lac-O1} -RBS1- <i>cat</i>	EQ4	constitutive expression of <i>cat</i> by the synthetic P _{Lac-O1} promoter at the <i>ycaD</i> locus; employs “RBS1” as the Shine-Dalgarno (SD) sequence*	EQ75
Cat2	Km ^r : <i>rrnBT</i> : P _{Ltet-O1} - <i>cat</i>	EQ4	constitutive expression of <i>cat</i> by the synthetic P _{Ltet-O1} promoter at the <i>ycaD</i> locus; employs RBS1 as SD sequence	EQ92
Cat3	<i>rrnBT</i> : P _{Lac-O1} -RBS3- <i>cat</i>	EQ4	as Cat1, but employs “RBS3” as the SD sequence	EQ94
Cat4	<i>rrnBT</i> :P _{Lac-O1} P _{Lac-O1} -RBS4- <i>cat</i>	EQ4	as Cat1, but employs “RBS4” as the SD sequence	EQ95
Cat5	<i>rrnBT</i> : P _{Lac-O1} -RBS5- <i>cat</i>	EQ4	as Cat1, but employs “RBS5” as the SD sequence	EQ96
Cat6	<i>rrnBT</i> : P _{Lac-O1} -RBS6- <i>cat</i>	EQ4	as Cat1, but employs “RBS6” as the SD sequence	EQ98
Cat1m	Δ motA, <i>rrnBT</i> : P _{Lac-O1} -RBS1- <i>cat</i>	EQ4m	as Cat1, but immotile	EQ107
GCat1m	<i>rrnBT</i> : P _{Lac-O1} -RBS1- <i>cat</i> , Δ motA, Km ^r : <i>rrnBT</i> :P _{Ltet-O1} - <i>gfp</i>	EQ4m	as Cat1m, but also harboring constitutive expression of <i>gfp</i> at the <i>intC</i> locus	EQ108

* See table S3 for ribosomal binding site “RBS” sequences

Table S2: Biochemical parameters related to the Cm-CAT system for strain Cat1

Parameter (units)	Description [§]	From literature, or measured	Fit from data	Predicted [†]
λ_0 (hr ⁻¹)	growth rate in the absence of Cm	0.62 ± 0.03^a	—	—
K_D (μM)	Cm-ribosome dissociation constant	$0.6 - 2.7^b$	—	1.3 ± 0.12^k
K_m (μM)	Michaelis constant for CAT enzyme	12^c	—	—
k_{cat} (s ⁻¹)	turnover number for CAT enzyme	600^c	—	—
κ (s ⁻¹)	membrane permeability to Cm	$0.37 - 7.5^d$	—	1.5^l
V_0 ($\mu\text{M}/\text{OD}_{600}/\text{s}$)	CAT activity in the absence of Cm	3.7 ± 0.3^e	—	—
I_{50} (μM)	half-inhibition conc.	—	5.5 ± 0.5^h	$2.8 - 12^k$
V_0/κ (mM)	CAT activity relative to permeability	—	5.8 ± 0.5^i 5.78 ± 0.08^j	$0.90 - 18^m$
MIC (μM)	min. inhibitory conc.	$950 \pm 50^{f,g}$	—	950 ± 10^n

[§] All *in vivo* quantities refer to Cat1 cells growing exponentially in minimal glucose medium with Cm unless otherwise indicated.

[†]These values are predicted using other parameter values listed on the two left columns; they are provided to illustrate consistency between model results and literature.

^a. Growth rate of strain Cat1 in glucose minimal media in absence of antibiotics, fit from slope of log-OD versus time with standard deviation from four replicates.

^b. The range of dissociation constant values reported for Cm-ribosome binding (22, 84).

^c. Michaelis constant and the turnover number for CAT enzyme (23). Error for the K_m value is described as “less than 10%” in the reference.

^d. Membrane permeability for Cm were estimated using the methods of Nikaido (88). Briefly, permeability of Cm through cytoplasmic membrane is calculated based on Cm hydrophobicity and molecular weight (97, 98). Permeability through *E. coli* outer membrane is calculated using available data for permeabilities of antibiotics of similar hydrophobicity, molecular weight, size and charge (85, 102, 103). Based on simple flux balance across each membrane, an effective permeability κ is defined in terms of cytoplasmic and outer membrane permeabilities using reported dimensions of cell volume and membrane surface area (88) (see expression [S46] and equation [S49] in supplement).

- e. V_0 , the CAT activity of exponentially growing Cat1 cells in Cm-free medium, is quantified using a spectrophotometric assay (77) (see Supplementary Methods). We provide the estimated *in vivo* activity here as acetylation rate per cytoplasmic volume by the following conversion. We divide the molar rate of Cm acetylated/OD₆₀₀ by a factor (112) of 1.6 to convert our measurements from per-OD₆₀₀ to per-OD₄₆₀, and then divide by cell volume per mass (113) of $0.34 \pm 0.04 \mu\text{L cells}/(\text{mL culture} \cdot \text{OD}_{460})$ to obtain the rate relative to equivalent cell volume in the reaction. Cell volume per mass changes little across strains or growth conditions in *E. coli* (113–115). We finally divide this quantity by 0.8 to take into account that cytoplasm comprises approximately 80% of total cell volume in *E. coli* K-12 (116, 117) to obtain the result in desired units: $V_0 \approx 8.5 \pm 0.8 \text{ mM/s}$.
- f. MIC from the abrupt growth rate drop in batch cultures. See, for example, growth curves in fig. S11.
- g. MIC_{plate} from LB plating, see fig. S2.
- h. The value of half-inhibitory concentration obtained from the fit of the growth data of wild type cells in sub-inhibitory concentrations of Cm (Fig. 3D) to equation [3], assuming $[\text{Cm}]_{\text{int}} \sim [\text{Cm}]_{\text{ext}}$. We performed a simple weighted least squares fit using weights $w = (\text{s.e.})^{-2}$ for each data point, with s.e. given by the standard error of doubling time for each determination (error bars in Fig. 3D). Uncertainty in the fit parameter I_{50} is a function of the estimated variance and is reported as standard error of the regressed parameter, with estimated variance $\sigma^2 = \sum_i w_i \cdot (\text{fit residual}_i)^2 / (\text{D.F.})$.
- i. Parameter V_0/κ is obtained from solving equation [S28] for with the empirical (batch culture) MIC obtained for strain Cat1, with the value MIC=950 μM taken from (f,g), the value of $I_{50} = 5.5 \mu\text{M}$ taken from (h), and K_m from (c). Error represents uncertainties propagated from MIC, I_{50} , and K_m .
- j. This is an alternative estimate obtained by fitting the growth rate data of Fig. 4A with an equation for $\lambda([\text{Cm}]_{\text{ext}})$ obtained from equations 1-3, with V_0/κ as the only free parameter (as described in fig. S17). To fit the data independently of MIC, data from non-growing cultures were excluded from fit and we used only the data for which growth rates were non-zero. This value obtained by fitting growth rates is similar to the value predicted by MIC in (f).
- k. The half-inhibitory concentration is expected to be proportional to the Cm-ribosome dissociation constant as discussed in the supplementary text ($I_{50} = K_D \lambda_{\text{max}}/\lambda_0$, equation [S5]), independent of a strain's CAT activity. To provide the value of K_D predicted by our model and growth data, we solve this equation for K_D using the fit value of $I_{50} = 5.5 \mu\text{M}$ from (h), $\lambda_0 = 0.67 \text{ hr}^{-1}$ for WT strain EQ4 from (a), and $\lambda_{\text{max}} = 2.85 \text{ hr}^{-1}$ from Scott *et al*⁹. Conversely, we also calculate an estimate for I_{50} using equation [S5] and the K_D range from the literature given in (b).
- l. We obtain this estimate $\kappa = 1.5 \text{ s}^{-1}$ from the $V_0/\kappa = 5.8 \text{ mM}$ obtained by MIC (f) and the *in vitro* value for V_0 reported in (e). In Fig. 4, we obtain the V_0/κ values for strains Cat2-Cat6 by assuming all strains have this same permeability to Cm. With this assumption, V_0/κ for all strains are determined simply by the relative CAT activities displayed in Figure 3B (grey bars).

- ^m. This estimate of the key parameter of the model uses the parameter values V_0 and κ given in (e) and (d) respectively.
- ⁿ. MIC calculated using the value of V_0/κ obtained from fitting our model to growth rates (j) and equation [S28] from the Main Text, with the value of $I_{50} = 5.5 \mu\text{M}$ taken from (h), and K_m from (c). Error propagated from standard error of fit in (j) and uncertainties of I_{50} and K_m .

Table S3: RBS substitutions

RBS ID	Strain	P _{Llac-01} and RBS
RBS1	Cat1	CTCGAGAATTGTGAGCGGATAACAATTGACATTGTGAGCGGA TAACAAGATACTGA GCACATCAGCAGGACGCACTGACCGAATTCATTAAAGAGGAG AAAGGTACCATG
RBS3	Cat3	CTCGAGAATTGTGAGCGGATAACAATTGACATTGTGAGCGGA TAACAAGATACTGA GCACATCAGCAGGACGCACTGACCGAATTCATTAAAGAGGAGT CCTAAAGGTACCATG
RBS4	Cat4	CTCGAGAATTGTGAGCGGATAACAATTGACATTGTGAGCGGA TAACAAGATACTGA GCACATCAGCAGGACGCACTGACCGAATTCATTAAAGAGGAC AAAGGTACCATG
RBS5	Cat5	CTCGAGAATTGTGAGCGGATAACAATTGACATTGTGAGCGGA TAACAAGATACTGA GCACATCAGCAGGACGCACTGACCGAATTCATTAAAGAGGAC TCCTAAAGGTACCATG
RBS6	Cat6	CTCGAGAATTGTGAGCGGATAACAATTGACATTGTGAGCGGA TAACAAGATACTGA GCACATCAGCAGGACGCACTGACCGAATTCATTAAAGAGGCC TCCTAAAGGTACCATG
		P _{Ltet-01} and RBS
RBS1	Cat2	CTCGAGTCCCTATCAGTGATAGAGATTGACATCCCTATCAGTG ATAGAGATACTGAGCACATCAGCAGGACGCACTGACCGAATT CATTAAAGAGGAGAAAGGTACCATG

Modifications of the RBS region in constitutive promoters. The -35 (TTGACA) and -10 (GATACT) elements are underlined and the transcriptional start site (+1; indicated a bolded capital “A”) and the first codon (ATG) are bolded. RBS is highlighted in cyan, nucleotide substitutions in yellow, and nucleotide insertion in magenta. RBS1=original RBS; RBS3=4 base insertion; RBS4=1-base substitution; RBS5= 1-bp substitution plus 4-base insertion; and RBS6=2-bp substitution plus 4-base insertion.

Table S4: Primers used in this study

Primer	Sequence (5' to 3')	Use
Cat-Kpn-F	ATAGGTACCATGGAGAAAAAATCACT GGATATAC	Cloning <i>cat</i> into pKDT_ P _{Lac-O1} or pKDT_P _{Ltet}
Cat-Bam-R	ATTGGATCCTTACGCCCCGCCCTGCCAC TC	Cloning <i>cat</i> into pKDT_ P _{Lac-O1} or pKDT_P _{Ltet}
tetA-Kpn-F	AATGGTACCATGAATAGTTCGACAAAG ATCGCATTG	Cloning <i>tetA</i> into pKDT_ P _{Lac-O1}
tetA-Bam-R	TATGGATCCTAAGCACTTGTCTCCTGTT TACTC	Cloning <i>tetA</i> into pKDT_ P _{Lac-O1}
Plac-RBS1	CATTGGGATATATCAACGGTGGTATAT CCAGTGATTTTTTCTCCATGGTACCTT TAGGACTCCTCTTTAATGAATTC	RBS region mutation in P _{Lac-O1}
Plac-RBS3	CATTGGGATATATCAACGGTGGTATAT CCAGTGATTTTTTCTCCATGGTACCTT TGTCCTCTTTAATGAATTC	RBS region mutation in P _{Lac-O1}
Plac-RBS4	CATTGGGATATATCAACGGTGGTATAT CCAGTGATTTTTTCTCCATGGTACCTT TAGGAGTCCTCTTTAATGAATTC	RBS region mutation in P _{Lac-O1}
Plac-RBS5	CATTGGGATATATCAACGGTGGTATAT CCAGTGATTTTTTCTCCATGGTACCTT TGGCCTCTTTAATGAATTC	RBS region mutation in P _{Lac-O1}
Plac-RBS6	CATTGGGATATATCAACGGTGGTATAT CCAGTGATTTTTTCTCCATGGTACCTT TAGGAGGCCTCTTTAATGAATTC	RBS region mutation in P _{Lac-O1}
PlaclacZ-P1	GCATTTACGTTGACACCATCGAATGGC GCAAACCTTTCGCGGTATGTGTAGGC TGGAGCTGCTTC	Chromosomal substitution of P _{Lac-O1} to <i>lacI</i> and PlacZYA
PlaclacZ-P2	CGTTGTAACGACGGCCAGTGAATCC GTAATCATGGTCATAGCTGTTTTCTCCT CTTTAATGAATTCGG	Chromosomal substitution of P _{Lac-O1} to <i>lacI</i> and PlacZYA
Lac-ver-R	CAACTGTTGGGAAGGGCGATCGGTG	Verification of chromosomal P _{Lac-O1}
Cat-P1	AGACGCGATGCATTGCTCTGAAAGCAT AGACGGGAAATATGAGTTTGCTGTGTA GGCTGGAGCTGCTTC	Chromosomal integration of P _{Lac-O1-cat} or P _{Ltet-cat} to <i>ycaD</i> locus
Cat-P2	GGTGAAAATACGCGATATCCAGCGGC GGTATTATCGATTTATATTACATGAGAA TTAATTCCGGGGATCC	Chromosomal integration of P _{Lac-O1-cat} or P _{Ltet-cat} to <i>ycaD</i> locus
<i>ycaD</i> -ver-R	GCCAGAGTCAACAAAAGCAGGC	Verification of chromosomal P _{Lac-O1-cat} or P _{Ltet-cat}

Table S5: Biochemical parameters related to the TetA system for Tc (top) and Mn (bottom)

Parameter (units)	Description	From literature, or measured	Fixed by MIC	Fit in model [*]	Predicted
λ_0 (hr ⁻¹)	growth rate in absence of antibiotic	0.68 ^a	—	—	—
K_d^{Tc} (μM)	Tc-ribosome binding dissociation constant	1 ^b	—	—	—
K_m^{Tc} (μM)	Michaelis constant for TetA pump and Tc	10 ^c	—	—	—
I_{50}^{Tc} (μM)	growth half-inhibition constant for Tc	—	—	3.6 ± 0.4 ^d	4.2 ^e
V_0 / κ_{Tc} (mM)	TetA-Tc activity relative to Tc permeability in strain Ta1	—	4.20 ± 0.30 ^f	4.41 ± 0.12 ^d 4.43 ± 0.08 ^g	—
K_d^{Mn} (μM)	Mn-ribosome binding dissociation constant	0.2 ^h	—	—	—
K_m^{Mn} (μM)	Michaelis constant for TetA pump and Mn	2 ⁱ	—	—	—
I_{50}^{Mn} (μM)	Growth half-inhibition constant for Mn	—	—	0.89 ± 0.1 ^j	0.84 ^k
V_0 / κ_{Mn} (μM)	TetA-Mn activity relative to Mn permeability in strain Ta1	—	368 ± 16 ^l	334 ± 22 ^j 324 ± 14 ^m	—

[§] All *in vivo* quantities refer to Cat1 cells growing exponentially in minimal glucose medium with indicated antibiotic unless otherwise noted.

^{*}“Fit in model” parameters show that fitting the model to empirical growth rates gives similar results to those predicted by MIC alone. The fit values for I_{50} also illustrate consistency with values calculated from *in vitro* data.

[†]These values are predicted using other parameter values listed in the far left column; they are provided to illustrate consistency between model results and predictions based on literature.

^a. Growth rate of strain Ta1 determined in glucose minimal media batch culture in absence of antibiotics

^b. The dissociation constant for Tc-ribosome binding to its single high-affinity site (83, 118). Some reports indicate a lower binding affinity, however this is likely due to an

inability to control for non-saturable binding in some experiments; see (83, 119) and references therein.

- c. Michaelis constant for TetA efflux of tetracycline (88).
- d. Here, the half-inhibitory concentration I_{50} and TetA activity V_0/κ were obtained by simultaneously fitting our model (equations [1]-[3]) to growth rate data of strain Ta1 growing in Tc, with K_m taken from (c), and λ_0 from (b). Errors are standard error of fit, and fitting procedures are identical to those used for Cm-CAT system described in fig. S15, except that we fit both V_0/κ and I_{50} simultaneously. See also equation [S60].
- e. The half-inhibitory concentration is expected to be proportional to the Tc-ribosome dissociation constant as discussed in the supplement ($I_{50} = K_D \cdot \lambda_{\max} / \lambda_0$, equation [S5]), independent of a strain's efflux activity, and is calculated here with K_D given in (b), $\lambda_0 = 0.68 \text{ hr}^{-1}$ of strain Ta1 given in (a), and $\lambda_{\max} = 2.85 \text{ hr}^{-1}$.
- f. This parameter is obtained by solving equation [S28] for V_0/κ with the empirical MIC obtained for strain Ta1 in Tc (MIC = $650 \pm 50 \mu\text{M}$, fig. S11A), the value of I_{50}^{Tc} taken from (e), and K_m from (c). Error represents uncertainties propagated from MIC.
- g. Here we fit V_0/κ as the only free parameter in our model to growth rate data of strain Ta1 growing in Tc with the value of I_{50}^{Tc} taken from (e), and K_m taken from (c). Errors are standard error of fit, and fitting procedures are identical to those used for Cm-CAT system described in fig. S16.
- h. The dissociation constant for Mn-ribosome binding is reported in table 2 of Olson *et al.* (119). We obtain a similar value from the relative binding-affinities of minocycline and tetracycline for 30S-ribosome, given by competitive binding assays between [^3H]-tetracycline and each compound (table 3 in Olson *et al.* (119)). EC_{50} for each compound gives the concentration at which [^3H]-tetracycline binding is reduced by 50% due to competitive binding. Then $K_D^{\text{Mn}} = \frac{\text{EC}_{50}^{\text{Mn}}}{\text{EC}_{50}^{\text{Tc}}} \cdot K_D^{\text{Tc}} = 0.2 K_D^{\text{Tc}}$, with K_D^{Tc} taken from (b).
- i. Michaelis constant for TetA efflux of minocycline is taken as the concentration of minocycline required to inhibit TetA-mediated influx of [^3H]-tetracycline into everted membrane vesicles by 50%, reported elsewhere (120, 121).
- j. The half-inhibitory concentration I_{50} and TetA activity V_0/κ for Mn are obtained as in note (e), except using growth rate data from growth in Mn, with K_m taken from (i).
- k. The half-inhibitory concentration is expected to be proportional to the Mn-ribosome dissociation constant as discussed in the supplement ($I_{50} = K_D \cdot \lambda_{\max} / \lambda_0$, equation [S5]), independent of a strain's efflux activity, and is calculated here with K_D given in (h).
- l. This parameter is obtained by solving equation [S28] for V_0/κ with the empirical MIC obtained for strain Ta1 in Mn (MIC $\approx 58 \pm 3 \mu\text{M}$, see Fig. 10B), the value of I_{50}^{Mn} taken from (k), and K_m from (i). Error represents uncertainties propagated from MIC.
- m. This V_0/κ was obtained by fitting our model as in note (g), except using growth rate data from growth in Mn with I_{50}^{Mn} taken from (k), and K_m from (i).

Supplementary References

71. K. A. Datsenko, B. L. Wanner, One-step inactivation of chromosomal genes in *Escherichia coli* K-12 using PCR products, *Proc. Natl. Acad. Sci. U. S. A.* **97**, 6640–5 (2000).
72. R. Lutz, H. Bujard, Independent and tight regulation of transcriptional units in *Escherichia coli* via the LacR/O, the TetR/O and AraC/I1-I2 regulatory elements, *Nucleic Acids Res.* **25**, 1203–10 (1997).
73. L. C. Thomason, N. Costantino, D. L. Court, in *Current protocols in molecular biology*, F. M. Ausubel, Ed. (John Wiley and Sons, Inc, New York, 2007), vol. Chapter 1, p. Unit 1.17.
74. W. Hillen, C. Berens, Mechanisms underlying expression of Tn10 encoded tetracycline resistance, *Annu. Rev. Microbiol.* **48**, 345–69 (1994).
75. E. Levine, Z. Zhang, T. Kuhlman, T. Hwa, Quantitative characteristics of gene regulation by small RNA, *PLoS Biol.* **5**, e229 (2007).
76. M. Kim *et al.*, Need-based activation of ammonium uptake in *Escherichia coli*, *Molecular Systems Biology* **8**, 616 (2012).
77. W. Shaw, Chloramphenicol Acetyltransferase from Chloramphenicol-Resistant Bacteria, *Methods in Enzymology* **43**, 737 (1975).
78. B. Seed, J. Y. Sheen, A simple phase-extraction assay for chloramphenicol acyltransferase activity, *Gene* **67**, 271–7 (1988).
79. J. H. Miller, *Experiments in Molecular Genetics* (Cold Spring Harbor Laboratory Press, New York, 1972), pp. 352–355.
80. E. R. Garrett, G. H. Miller, Kinetics and Mechanisms of Action of Antibiotics on Microorganisms III, *J. Pharm. Sci.* **54**, 427–431 (1965).
81. S. Comby, J. P. Flandrois, G. Carret, C. Pichat, Mathematical modelling of bacterial growth at subinhibitory levels of aminoglycosides, *Annales de l'Institut Pasteur Microbiology* **139**, 613–629 (1988).
82. S. Comby, J. Flandrois, G. Carret, C. Pichat, Mathematical Modelling Of Growth Of *Escherichia Coli* At Subinhibitory Levels Of Chloramphenicol Or Tetracyclines, *Research in Microbiology* **140**, 243–254 (1989).
83. B. Epe, P. Woolley, The binding of 6-demethylchlortetracycline to 70S, 50S and 30S ribosomal particles: a quantitative study by fluorescence anisotropy, *The European Molecular Biology Organization Journal* **3**, 121–126 (1984).

84. A. Contreras, D. Vázquez, Cooperative and antagonistic interactions of peptidyl-tRNA and antibiotics with bacterial ribosomes, *European Journal of Biochemistry /FEBS* **74**, 539–47 (1977).
85. H. Nikaido, D. G. Thanassi, Penetration of Lipophilic Agents with Multiple Protonation Sites into Bacterial Cells : Tetracyclines and Fluoroquinolones as Examples, *Antimicrob. Agents Chemother.* **37**, 1393–1399 (1993).
86. R. E. Hancock, A. Bell, Antibiotic uptake into gram-negative bacteria, *European Journal of Clinical Microbiology and Infectious Diseases* **7**, 713–20 (1988).
87. L. M. McMurry, D. a Aronson, S. B. Levy, Susceptible Escherichia coli cells can actively excrete tetracyclines, *Antimicrob. Agents Chemother.* **24**, 544–51 (1983).
88. D. G. Thanassi, G. S. B. Suh, H. Nikaido, Role of Outer Membrane Barrier in Efflux-Mediated Tetracycline Resistance of Escherichia coli, *Microbiology* **177**, 998–1007 (1995).
89. H. Nikaido, S. Normark, Sensitivity of Escherichia coli to various beta-lactams is determined by the interplay of outer membrane permeability and degradation by periplasmic beta-lactamases: a quantitative predictive treatment, *Mol. Microbiol.* **1**, 29–36 (1987).
90. E.-B. Goh *et al.*, Transcriptional modulation of bacterial gene expression by subinhibitory concentrations of antibiotics, *Proc. Natl. Acad. Sci. U. S. A.* **99**, 17025–30 (2002).
91. E. Rotem *et al.*, Regulation of phenotypic variability by a threshold-based mechanism underlies bacterial persistence, *Proc. Natl. Acad. Sci. U. S. A.* **107**, 12541–6 (2010).
92. K. Nordström, L. C. Ingram, a Lundbäck, Mutations in R factors of Escherichia coli causing an increased number of R-factor copies per chromosome, *J. Bacteriol.* **110**, 562–9 (1972).
93. P. G. S. Mortimer, L. J. V Piddock, The accumulation of five antibacterial agents in porin-deficient mutants of Escherichia coli, *J. Antimicrob. Chemother.* **32**, 195–213 (1993).
94. X. Z. Li, D. M. Livermore, H. Nikaido, Role of efflux pump(s) in intrinsic resistance of Pseudomonas aeruginosa: resistance to tetracycline, chloramphenicol, and norfloxacin, *Antimicrob. Agents Chemother.* **38**, 1732–41 (1994).
95. D. J. Novo, N. G. Perlmutter, R. H. Hunt, H. M. Shapiro, Multiparameter Flow Cytometric Analysis of Antibiotic Effects on Membrane Potential , Membrane Permeability , and Bacterial Counts of Staphylococcus aureus and Micrococcus luteus, *Antimicrob. Agents Chemother.* **44**, 827–834 (2000).
96. C. Gauthier, Y. St-pierre, R. Villemur, Rapid antimicrobial susceptibility testing of urinary tract isolates and samples by flow cytometry, *Journal of Medical Microbiology* **51**, 192–200 (2002).
97. R. Collander, The Permeability of Nitella Cells to Non-Electrolytes, *Physiol. Plant.* **7**, 420–445 (1954).
98. Q. R. Bartz, Isolation and Characterization of Chloromycetin, *J. Biol. Chem.* **172**, 445–450 (1948).

99. W. Stein, *The movement of molecules across cell membranes* (Academic Press, Inc, New York, 1967).
100. D. Pramer, Absorption of antibiotics by plant cells IV. Chloramphenicol, *Exp. Cell Res.* **16**, 70–74 (1959).
101. H. Nikaido, Molecular basis of bacterial outer membrane permeability revisited, *Microbiol. Mol. Biol. Rev.* **67** (2003), doi:10.1128/MMBR.67.4.593.
102. H. Nikaido, E. Rosenberg, J. Foulds, Porin channels in Escherichia coli: studies with beta-lactams in intact cells, *J. Bacteriol.* **153**, 232 (1983).
103. F. Yoshimura, H. Nikaido, Diffusion of beta-lactam antibiotics through the porin channels of Escherichia coli K-12, *Antimicrob. Agents Chemother.* **27**, 84–92 (1985).
104. C. Wu, P. Clift, C. H. Fry, J. A. Henry, Membrane action of chloramphenicol measured by protozoan motility inhibition, *Arch. Environ. Contam. Toxicol.* , 850–853 (1996).
105. A. J. Griffiths, J. H. Miller, D. T. Suzuki, R. C. Lewontin, W. M. Gelbart, in *An Introduction to Genetic Analysis*, (W. H. Freeman, New York, 2000).
106. G. N. Rolinson, a C. Macdonald, D. a Wilson, Bactericidal action of beta-lactam antibiotics on Escherichia coli with particular reference to ampicillin and amoxycillin, *J. Antimicrob. Chemother.* **3**, 541–53 (1977).
107. D. Shah *et al.*, Persisters: a distinct physiological state of E. coli, *BMC Microbiology* **6**, 53 (2006).
108. H. Luidalepp, A. Jöers, N. Kaldalu, T. Tenson, Age of inoculum strongly influences persister frequency and can mask effects of mutations implicated in altered persistence, *J. Bacteriol.* **193**, 3598–605 (2011).
109. B. J. Paul, W. Ross, T. Gaal, R. L. Gourse, rRNA transcription in Escherichia coli, *Annu. Rev. Genet.* **38**, 749–70 (2004).
110. M. Schaechter, O. Maaløe, N. O. Kjeldgaard, Dependency on medium and temperature of cell size and chemical composition during balanced growth of Salmonella typhimurium, *Journal of General Microbiology* **19**, 592–606 (1958).
111. I. Chopra, K. Hacker, Z. Misulovin, D. M. Rothstein, Sensitive Biological Detection Method for Tetracyclines Using a tetA-lacZ Fusion System, *Antimicrob. Agents Chemother.* **34**, 111–116 (1990).
112. M. Bipatnath, P. P. Dennis, H. Bremer, Initiation and velocity of chromosome replication in Escherichia coli B/r and K-12, *J. Bacteriol.* **180**, 265–73 (1998).
113. G. Churchward, E. Estiva, H. Bremer, Growth rate-dependent control of chromosome replication initiation in Escherichia coli, *J. Bacteriol.* **145**, 1232–8 (1981).

114. K. Begg, W. Donachie, Changes in cell size and shape in thymine-requiring *Escherichia coli* associated with growth in low concentrations of thymine, *J. Bacteriol.* **133**, 452–8 (1978).
115. H. Bremer, P. P. Dennis, in *Escherichia coli and Salmonella typhimurium: cellular and molecular biology*. American Society for Microbiology, Washington, DC, (1987), pp. 1527–1542.
116. S. Cayley, B. A. Lewis, H. J. Guttman, M. T. Record, Characterization of the cytoplasm of *Escherichia coli* K-12 as a function of external osmolarity. Implications for protein-DNA interactions in vivo, *J. Mol. Biol.* **222**, 281–300 (1991).
117. J. Stock, B. Rauch, S. Roseman, Periplasmic space in *Salmonella typhimurium* and *Escherichia coli*, *J. Biol. Chem.* **252**, 7850–7861 (1977).
118. M. Buck, B. Cooperman, Single protein omission reconstitution studies of tetracycline binding to the 30S subunit of *Escherichia coli* ribosomes, *Biochemistry* **29**, 5374–5379 (1990).
119. M. W. Olson *et al.*, Functional, Biophysical, and Structural Bases for Antibacterial Activity of Tigecycline, *Antimicrob. Agents Chemother.* (2006), doi:10.1128/AAC.01499-05.
120. J. Bergeron *et al.*, Glycylcyclines bind to the high-affinity tetracycline ribosomal binding site and evade Tet(M)- and Tet(O)-mediated ribosomal protection, *Antimicrob. Agents Chemother.* **40**, 2226–2228 (1996).
121. M. L. Nelson *et al.*, Inhibition of the tetracycline efflux antiport protein by 13-thio-substituted 5-hydroxy-6-deoxytetracyclines, *J. Med. Chem.* **36**, 370–377 (1993).